

Micromodeling of Aerospace Structural Alloys

FAA: 98-G-018 Task J

Final Report
1999-2000

B.J. Yang, R. Ruxanda, and D.M. Stefanescu

Solidification Laboratory and
Metal Casting Technology Center
The University of Alabama
Tuscaloosa, Alabama

Contents

1. Executive summary	4
2. Introduction	5
3. Modeling of microstructural evolution	5
3.1 Macrotransport model	6
3.1.1 Assumptions in macrotransport model	6
3.1.2 Governing equations and formulation	7
3.1.3 Viscosity and permeability	10
3.1.4 Solution method	11
3.2 Microtransport model	13
3.2.1 Algorithm of nucleation rate	13
3.2.2 Algorithm of growth velocity	14
3.2.3 Tracking of grains	15
3.2.4 Distribution of grain size	16
3.2.5 Competitive growth and non-equilibrium solidification	18
3.2.6 Segregation models	19
3.3 Coupling of macro- and micro-modeling	21
3.3.1 Coupling problems	21
3.3.2 Numerical procedure	21
4. Determination of the thermophysical properties	23
4.1 Possible approaches	23
4.2 Comparison between various approaches	28
4.3 Summary of relationships for A356 and D357 alloys	30
5. Model verification	30
5.1 Design of test sample and its boundary conditions	30
5.2 Implementation on A356 and D357	30
5.3 Case study	36
5.4 Comparisons	37
5.4.1 Nastac-Stefanescu model and Scheil model	37

5.4.2 Between A356 and D357	40
6. Possible model improvements	41
6.1 Consideration of the eutectic modification process	41
6.2 Nucleation and growth of dendritic grains	44
6.3 Average grain size	44
7. Experimental evaluation	46
7.1 The first test casting and instrumentation	46
7.2. The second test casting in the sand mold	47
7.2.1 Casting sample and thermocouple positions	47
7.2.2 Cooling curves and discussion	48
7.2.3 Macrostructure and microstructure	49
7.3 Samples poured in a metal mold	50
7.3.1 The first metal mold and instrumentation	50
7.3.2 Typical cooling curves in the metal mold	51
7.3.3 Microstructure observation	52
7.3.4 Thermal analysis	53
7.4 Measurement of grain density	56
7.5 Quenching experiment and microstructure observation	57
7.6 Visualization of eutectic grains	57
7.6.1 Chemical etching	58
7.6.2 Thermal etching	58
8. Conclusions	60
9. Future work	61
References	62

1. Executive summary

A comprehensive model for prediction of microstructure evolution of multi-component alloys with equiaxed dendritic and eutectic morphology was developed. The model can account for the effects of natural convection, solidification contraction, solidification kinetics and grain movement on the microstructure evolution during solidification.

The novelty of this approach is that the model includes tracking of dendritic and eutectic grains during solidification, and that it eliminates the assumption of uniform grain size in a given volume element, which is standard in current solidification models.

The computed results show that the tracking of grain movement is important to accurately predict the microstructure evolution and final microstructural characteristics.

The proposed model is designed to be used for the prediction of microstructure features of A356 and D357 alloys when the database is available.

The proposed model has improved on existing models by using continuous nucleation and a grain distribution function over the volume element, in addition to solid transport.

To track grain movement, rules of grain movement were proposed. The method allows tracking grain growth of continuously nucleated grains and their movement without using large amounts of computer memory. It is a practical approach that can be used for large castings where the number of control volumes is high.

The proposed model deals with the non-equilibrium solidification and competitive growth has been introduced in the program.

An equivalent pseudo-binary alloy system was proposed to obtain the liquidus temperature of A356 and D357 alloys. The results are very close to those obtained from the multi-component alloy system. This is an efficient method to deal with multi-component alloys.

A significant amount of experimental work has been performed with the purpose of establishing correct nucleation and growth laws for dendritic and eutectic solidification in the multicomponent alloys of interest (A356 and D357). However, more experiments are needed to complete this task.

The present model is two-dimensional. To correctly describe solidification of commercial castings, a three-dimensional version must be developed.

2. Introduction

The project undertaken was designed to supplement and support work at Northwestern University under the direction of Prof. James Conley. The basic premise of the program is to develop methodology so that aluminum and titanium alloy castings can be designed for both inspectability and performance. This can be accomplished using principles of solidification to predict the probability of formation of casting defects during solidification and subsequent cooling. The microstructure and the defects determine the mechanical properties of the casting.

This report will describe the progress made during the first year of the *Micromodeling of Aerospace Structural Alloys* research. The research project has two major parts, that is, Modeling of Microstructural Evolution and Experimental Evaluation.

The main effort during the first year was devoted to the modeling of microstructural evolution of A356 and D357 alloys. Limited experimental work for the parameter evaluation of solidification kinetics was initiated in the last quarter of the year.

The role that The University of Alabama played in this program was to model the solidification kinetics such as the nucleation and growth of solid aluminum alloy phases from the liquid, including the Al-Si eutectic found in A356 and D357 alloys, and the nucleation and growth of titanium alloy phases in Ti-6Al-4V alloy. Nucleation and growth models are crucial to the accurate prediction of as-cast microstructure, and thus to the successful attainment of program goals.

The goals of this program are as follows:

1. Develop comprehensive solidification models for A356, D357 and Ti-6Al-4V alloys
2. Perform experimental evaluation for data acquisition
3. Validate proposed models
4. Supply models to Prof. Conley for use in his work
5. Incorporate proposed models into commercial code
6. Validate commercial code predictions against the generated experimental data on solidification

The tasks for the first year are as follows:

1. Develop a general and comprehensive model to accurately predict the microstructural evolution for A356 and D357
2. Determine the solidification parameters of A356 and D357 alloys
3. Implement the proposed model for general model interrogation
4. Initiate experimental evaluation of nucleation laws for primary and eutectic phases of A356 alloy

3. Modeling of microstructural evolution

The modeling of microstructure evolution, which is now incorporated in a number of commercial codes, grew out of the need to model the generation of latent heat of fusion in alloy solidification more accurately. The evolution of latent heat in alloy solidification

depends on the fraction of solid at temperatures between the liquidus and solidus temperatures; this, in turn, depends on the nucleation and growth of the solid. As a result of work to determine latent heat, models have been developed which not only predict cast microstructure, but also map dendrite arm spacing, macrosegregation, and even the effect of subsequent heat treatment.

Because microstructure determines properties, prediction of microstructure makes prediction of properties possible. To date, three kinds of approaches are available to model microstructure evolution. The first generation models solve the heat conduction combined with solidification kinetics, but only consider the energy transport, and assume that the grains are fixed. They are mass-closed models. The second generation models include liquid flow in the macro-transport coupled with solidification kinetics. The solid grains are still assumed fixed during solidification. The third generation models solve macro-transport with liquid and solid flow coupled with solidification kinetics. Obviously, the third generation models are better to describe real solidification processes, and thus were selected for this work.

Several challenges may be anticipated. The first one is to describe the nucleation in the modeling over the whole solidification interval. The alloys of interest have a wide solidification interval, so that the instantaneous nucleation model is not good for A356 and D357 alloys. The second challenge is to describe how the heterogeneous nucleation is affected by natural convection and solidification shrinkage. The third is to model the eutectic phase and its competitive growth with the primary phase. This is of importance in aluminum-silicon alloys such as A356 and D357, where the morphology of the silicon eutectic can affect mechanical properties, and may well nucleate gas porosity. The proposed model will handle major phenomena occurring during solidification.

In general, the solidification of castings is driven by several physical phenomena, such as natural convection caused by the thermosolutal buoyancy, nucleation and growth of grains due to the undercooling of melt, solidification shrinkage due to the different densities between liquid and solid, and grain movement induced by melt convection and shrinkage. These phenomena strongly affect the solidification behavior of casting. Thus, it is very important to deal with those phenomena in micro-modeling.

The model has two basic components, macro-transport and micro-transport. The macro-transport describes the mass, energy, species and momentum transport, and the micro-transport deals with solidification kinetics and grain movement.

3.1 Macro-transport model

3.1.1 Assumptions in macro-transport model

In this work only equiaxed solidification was considered. The following basic assumptions have been used in the macro-transport model:

- (a) only liquid and solid phases are present (i.e. L, S, L+S, no pore formation);
- (b) the properties of the liquid and solid phases are homogeneous and isotropic;
- (c) no reaction exists among the solid grains during solidification;
- (d) there are two stages in the solidification process:

stage I: equiaxed grains move freely with the liquid, i.e., velocity of L/S mixture = velocity of solid = velocity of liquid; the viscosity of the mixture is described by a relative velocity; Darcy flow is not important;

stage II: a rigid dendritic skeleton is established (dendrite coherency is reached) and the velocity of the solid = 0 (the solid does not convect); the viscosity value returns to liquid viscosity; Darcy flow becomes significant;

(e) no relative velocity between the solid and liquid in the first stage of solidification.

(f) the liquid flow is driven by thermal and solutal buoyancy, as well as by solidification contraction.

3.1.2 Governing equations and formulation

The continuum approach was chosen to describe the macro-transport. In this method, only one set of transport equations is required to solve the mass, energy, species and momentum transport in the entire domain that consists of solid, liquid and mushy zone. The need to track the interface boundary is eliminated. Thus, all quantities are continuous in the entire domain. In the continuum model, each finite volume can be occupied by the liquid and solid phases simultaneously (two-phase system). The quantities of the system can be regarded as continuous and differentiable functions of time and space, and can be calculated as follows:

$$\text{Eq. 1} \quad g_L + g_S = 1 \quad \text{and} \quad f_L + f_S = 1$$

$$\text{Eq. 2} \quad f_L = \frac{g_L \rho_L}{\rho}$$

The average values over every volume element in the continuum approach, like density, thermal conductivity, and diffusivity, are defined as follows:

$$\text{Eq. 3} \quad \rho = g_S \rho_S + g_L \rho_L \quad k = g_S k_S + g_L k_L$$

$$\text{Eq. 4} \quad D = g_S D_S + g_L D_L$$

Additionally, velocity is defined as:

$$\text{Eq. 5} \quad \mathbf{V} = f_S \mathbf{V}_S + f_L \mathbf{V}_L$$

where subscripts S and L denote solid and liquid, respectively, g is the volume fraction, f is the mass fraction, ρ is averaged density of solid-liquid mixture, k is the thermal conductivity, \mathbf{V} is the average velocity, and D is the diffusion coefficient.

In the present model, the entire solidification process is divided in two stages. In the first stage, the solid equiaxed dendrites are moving freely with the flowing liquid, and no relative velocity exists between solid and liquid phase. In the second stage, there is no solid movement because of the continuous and fixed dendritic network. Therefore, using the classic mixture theory and the assumptions mentioned above, the simplified macroscopic transport equations derived by Bennon and Incropera¹ on the basis of the continuum model, can be used as follows:

Continuity

$$\text{Eq. 6} \quad \frac{\partial \rho}{\partial t} + \nabla \cdot (\rho \mathbf{V}) = 0$$

The first term of this equation indicates the shrinkage-induced flow described by the term $\frac{\partial \rho}{\partial t}$. Liquid flow will be driven toward a volume element when the average density increases with time. In this research, this increment is motivated by two issues:

1. as a result of solidification shrinkage, because solid density is higher than liquid density for aluminum-based hypoeutectic alloys;
2. as a result of solute-enriched liquid or difference in temperature, because the density is variable with the composition and temperature.

Momentum

x-momentum

$$\text{Eq. 7} \quad \frac{\partial}{\partial t}(\rho u) + \nabla \cdot (\rho \mathbf{V} u) = \nabla \cdot \left(\mu^* \nabla \frac{\rho}{\rho_L} u \right) - \frac{\partial p}{\partial x} - \nabla \cdot (\rho f_L f_s \mathbf{V}_r u_r) - \frac{\mu^*}{K} (u - u_s) - \frac{C_L \rho^2}{K^{1/2} \rho_L} |u - u_s| (u - u_s)$$

y-momentum

$$\text{Eq. 8} \quad \frac{\partial}{\partial t}(\rho v) + \nabla \cdot (\rho \mathbf{V} v) = \nabla \cdot \left(\mu^* \nabla \frac{\rho}{\rho_L} v \right) - \frac{\partial p}{\partial y} - \nabla \cdot (\rho f_L f_s \mathbf{V}_r v_r) - \frac{\mu^*}{K} (v - v_s) - \frac{C_L \rho^2}{K^{1/2} \rho_L} |v - v_s| (v - v_s) + g[\rho - \rho_0]$$

where p is the hydrostatic pressure, μ^* is the relative viscosity, K is permeability, \mathbf{V} is a velocity vector and can be expressed as $\mathbf{V} = f_s \mathbf{V}_s + f_L \mathbf{V}_L$, $\mathbf{V}_r (= \mathbf{V}_L - \mathbf{V}_s)$ and $u_r (= u_L - u_s)$ and v_r are the relative velocities between solid and liquid phases, in the x- and y-direction, respectively. ρ_L and ρ are densities of the liquid phase and the mushy zone respectively, and f_s and f_L are mass fractions of solid and liquid.

To solve the momentum equations, the first term on the right-hand side (RHS) of the y-momentum equation, for example, is separated in two terms, resulting in the following expression:

$$\text{Eq. 9} \quad \nabla \cdot \left(\mu^* \nabla \frac{\rho}{\rho_L} v \right) = \nabla \cdot \left(\mu^* \frac{\rho}{\rho_L} \nabla v \right) + \nabla \cdot \left(\mu^* v \nabla \frac{\rho}{\rho_L} \right)$$

The second term in Eq. 9 is used as a part of the source term in the solution of the momentum equations. A similar expression can be obtained for the x-momentum equation with the corresponding substitution of v for u . The other part of the source term in the

momentum equation comes from all the terms following and including the second term on the RHS of Eq. 8, the pressure contribution. Nevertheless, the pressure component receives a special treatment, which will be discussed later.

The third term on the RHS of the momentum equations describes the contribution of the relative motion between liquid and solid. It will be zero in the first stage because solid and liquid are moving with the same velocity. Clearly, this term is zero in the liquid stage because the solid fraction is zero.

The fourth and fifth terms in the RHS of Eq. 7 and Eq. 8 represents the drag force for the flow in the mushy zone, that is, Darcy flow. Thus, this term will be zero in the liquid and in the first stage.

The last term on the RHS of the y-momentum equation describes the thermosolutal effects using the gravity vector. This term can be substituted by the so-called Boussinesq approximation. Nevertheless, this approximation was not used here because the relationship between density and temperature is known. This term is not used for the x-momentum equation because when the x-direction is perpendicular to the gravity vector its component is eliminated.

Energy

$$\text{Eq. 10} \quad \frac{\partial}{\partial t}(\rho C_p T) + \nabla \cdot (\rho C_p V T) = \nabla \cdot (k \nabla T) - \nabla \cdot (L \rho_s g_s (V - V_s)) \\ - \frac{\partial}{\partial t}(L \rho_s g_s) - \nabla \cdot (L \rho_s g_s V)$$

The second term on the RHS of Eq. 10 is obtained to consider the contribution of the energy flux associated with the relative motion of the phases. Obviously, this term is zero in the first stage, because the solid and liquid have the same velocity. Also, it is zero in the liquid state where no variation of solid fraction occurs.

The third RHS term is associated with the liberation of latent heat during the solidification process and remains from the start of solidification to the end of the solidification. The fourth RHS term accounts for the influence of the general velocity on the evolution of the latent heat resulting from the generation of solid fraction. This term also exists during the whole solidification processes, like the third one.

During the first stage, because the relative velocity is zero, Eq. 10 is rewritten as:

$$\text{Eq. 11} \quad \frac{\partial}{\partial t}(\rho C_p T) + \nabla \cdot (\rho C_p V T) = \nabla \cdot (k \nabla T) - \frac{\partial}{\partial t}(L \rho_s g_s) - \nabla \cdot (L \rho_s g_s V)$$

The source term of Eq. 11 is made of the last two terms in the RHS.

During the second stage, because the solid velocity is zero, the same equation was rewritten as:

$$\text{Eq. 12} \quad \frac{\partial}{\partial t}(\rho C_p T) + \nabla \cdot (\rho C_p V T) = \nabla \cdot (k \nabla T) + \frac{\partial}{\partial t}(L \rho_s g_s)$$

The last term on the RHS of Eq. 12 is the source term.

Species

$$\text{Eq. 13} \quad \frac{\partial}{\partial t}(\rho C) + \nabla \cdot (\rho C V) = \nabla \cdot (\rho D \nabla C) + \nabla \cdot (\rho D \nabla (C_L - C)) - \nabla \cdot (\rho f_s (V - V_s)(C_L - C_s))$$

The first two terms on the RHS of the equation represent the total net diffusion of species. The third term describes the mass flux due to the relative movement of phases. This term can be eliminated in the first stage because the relative velocity is zero. The source term of this equation corresponds to the last two terms in the RHS of Eq. 13.

3.1.3 Viscosity and permeability

In the proposed model, small equiaxed grains can nucleate and grow in an undercooled melt in the early stage of solidification. The solid-liquid mixture can be considered as a slurry where dendritic grains are suspended in viscous molten liquid and can move with the liquid without interacting with one another. Thus, the variation of the viscosity of the mixture as a function of solid fraction can be described through a relative viscosity equation. The development of the equation for relative viscosity used in the current model has been described elsewhere². The empirical equation for the viscosity of the mixture is

$$\text{Eq. 14} \quad \mu^* = \mu_L \left[1 - \frac{F_\mu g_s}{0.3} \right]^{-2} \quad \text{with}$$

$$F_\mu = 0.5 - \frac{1}{\pi} \tan^{-1} [100(g_s - g_{cr})]$$

where F_μ is a switching function and g_{cr} is the critical solid fraction.

For equiaxed grains, the permeability can be regarded as isotropic. Thus, a permeability function can be obtained on the basis of the theory of flow through a porous medium. Accordingly, the Carman-Kozeny equation³ is used:

$$\text{Eq. 15} \quad K = \frac{g_L^3}{c(1 - g_L)^2 F_k}$$

where K is permeability, F_k is another switching function ($F_k = 1 - F_\mu$), and c is a function of dendrite dimension and can be expressed as $c = 180/d^2$ (d is a secondary dendrite arm spacing).

Figure 1 demonstrates the switching function. It can be seen that when the solid fraction is less than g_{cr} , the value of F_μ is close to unity, while it is equal to zero when the solid fraction is larger than g_{cr} . It indicates that the viscosity of mixture is employed in the first stage of solidification and then turned off in the second stage. Conversely, permeability is shut off in the first stage and turned on in the second stage.

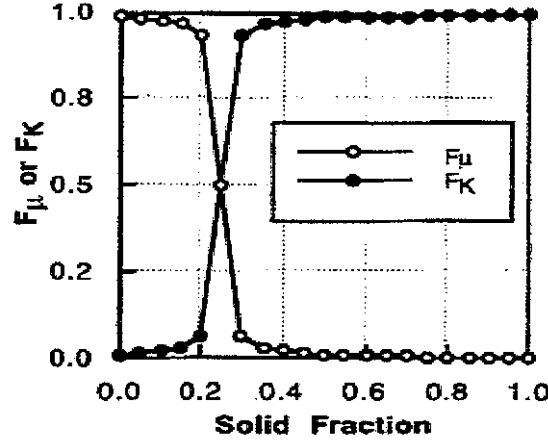


Figure 1 Demonstration of the switching functions

When the solid phase is moving with the liquid in the first stage, the relative viscosity increases continuously as the solid fraction increases. The permeability coefficient is assumed to be infinity. In the second stage of solidification the relative viscosity becomes the liquid viscosity.

3.1.4 Solution method

The method used to solve the momentum equations was the Semi-Implicit Method for Pressure-Linked Equations-Revised (SIMPLER) algorithm. The upwind scheme was used to evaluate the convection term in the transport equations. The mass and energy equations can also be solved in a similar manner. To use the SIMPLER algorithm, it is necessary to write the conservation equations in the generalized format. In the continuum formulation, the macroscopic transport equations can be generalized as:

Eq. 16
$$\frac{\partial}{\partial t}(\rho \cdot \phi) + \nabla \cdot (\rho \mathbf{V} \phi) = \nabla \cdot (\Gamma \cdot \nabla \phi) + S$$

The term ϕ represents the phase quantity, Γ is the general diffusion coefficient, and S denotes the source term. For each of macro-transport equations, the specific quantities are illustrated in Table 1.

Table 1 Explanation of the quantities in Eq. 16

Transport Equation	ϕ	Γ	S
Mass	1	0	Source Term
Energy	$C_p \cdot T$	α	Source Term
Momentum	u or v	$\mu^* \frac{\rho}{\rho_L}$	Source Term
Species	C	$\rho \cdot D$	Source Term

The procedure to calculate the fluid flow is as follows:

1. Start with a guessed velocity field; this field gives the initial conditions, starting the program.
2. Calculate the coefficients for the momentum equations considered in the problem, in this case, X- and Y-momentum equations because the model is in two dimensions (2-D model), and calculate the so-called pseudo-velocities \hat{u} and \hat{v} , respectively.
3. Calculate the coefficients for the pressure equation using the actualized values of velocities from step 2, and solve the pressure equation to obtain the pressure field, p^* ; this pressure field is an intermediate field used to correct and solve the velocity field.
4. Use the p^* from step 3 and solve the momentum equations to obtain u^* and v^* .
5. Calculate the mass source, and the coefficients for the pressure equation and solve it to obtain the pressure field, p' , using the actualized velocities from step 4. This pressure field is called the pressure-correction.
6. Correct the velocity field by using the pressure-correction field from the previous step, but do not correct the pressure.
7. Return to step 2, using the velocity field as the guessed velocities, and repeat until convergence.

More details about this procedure and the way to solve the equations can be found in the literature⁴.

From step 3 to 7, convergence criteria are used in each step. For pressure, the convergence criterion is that the relative pressures between two successive computations must be equal or less than 10^{-4} . For velocities, the convergence criterion is that the relative velocities between two successive computations must be equal or less than 10^{-5} .

After convergence is obtained for the velocity field, the time is incremented and the actual velocities are used to calculate the temperature and composition fields. The loop is repeated until the liquid is no longer able to flow. The time step used is 10^{-3} sec. To solve the solidification problem of the samples of aluminum-based alloys, a uniform mesh of 10^{-3} m was used.

The procedure to calculate the temperature field is as follows:

1. Start with a initial temperature field, or the previous temperature field is used as an initial condition.
2. Calculate the source term by implementing the micro-transport model.
3. Calculate the temperature by substituting the values of the neighbor temperature and use an iterative procedure to obtain the value for each representative node, solving the energy equation.
4. Update the thermophysical properties, such as density, conductivity, etc.
5. Return to step 2 and repeat until convergence.

The same procedure is employed to calculate the composition field after the temperature converges. The convergence criterion is that the relative difference in temperature within

each time step must be equal or less than 10^{-5} , and the relative difference in composition must be equal or less than 10^{-5} .

The calculation of the source term is related to the micro-transport model. The coupling between macro-transport and micro-transport is through the source term in the macro-transport equation. The macro-transport and micro-transport should be solved simultaneously. The detailed description about the handling of the release of latent heat and calculation of solid fraction will be presented in the micro-transport model.

3.2 Micro-transport model

The basic elements of the microscopic solidification model include nucleation models for dendrites and eutectic grains, growth models for dendrites and eutectic, and tracking of grain movement. For macro-transport, the micro-transport will provide the heat flux due to the latent heat of fusion and the fraction of solid.

3.2.1 Algorithm of nucleation rate

For commercial casting alloys of interest nucleation occurs on heterogeneous substrates. Two empirical nucleation models, based on the heterogeneous nucleation theory, have been proposed. They rely heavily on metal- and process-specific experimental data. The continuous nucleation law (Figure 2b) assumes that the nucleation occurs at a certain undercooling, and new families of nuclei are generated successively as undercooling increases during solidification. The instantaneous nucleation law (Figure 2a) assumes that all nuclei are generated at a specific nucleation undercooling, and that the number of nuclei keeps constant during the entire solidification process. This is a site saturation model.

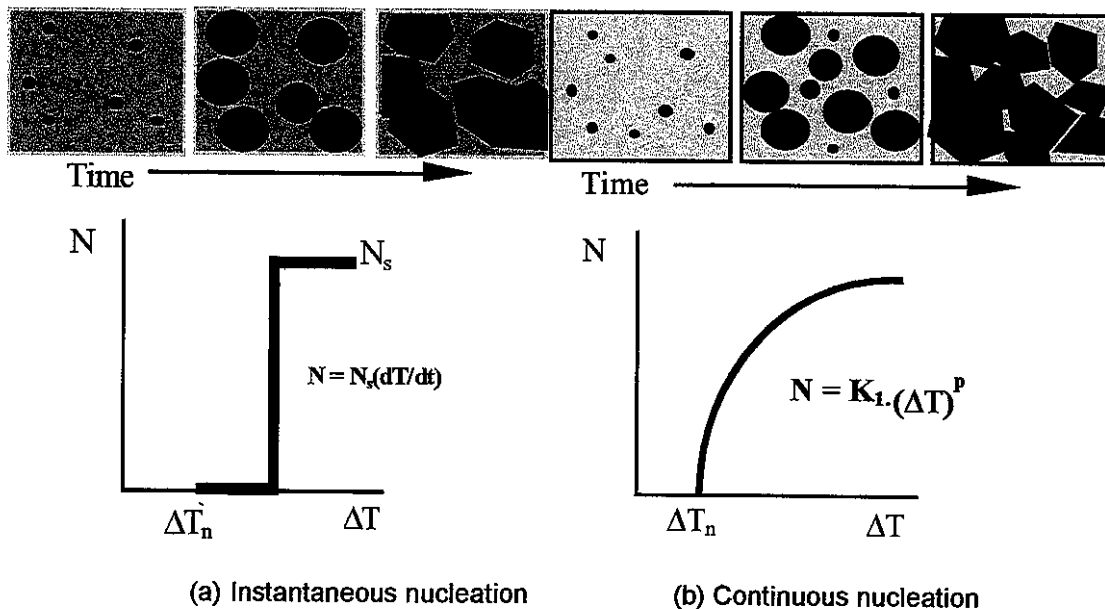


Figure 2 Schematic representation of two different nucleation laws

In general, the continuous nucleation law is suitable for all kinds of alloys, while the instantaneous nucleation is recommended for the pure metal and alloys with a narrow solidification interval. For the alloys of interest, A356 and D357, the solidification intervals are around 40-50 °C. Accordingly, the continuous nucleation was chosen in spite

of its complexity for modeling. The general expression of the continuous heterogeneous nucleation rate can be written as⁵:

$$\text{Eq. 17} \quad \frac{\partial N_h}{\partial t} = K_1 \cdot \Delta T^{p-1} \cdot \frac{\partial T}{\partial t}$$

where K_1 and p are parameters that depend upon the alloy type, nucleation potential and cooling rate. They must be evaluated experimentally. T is temperature, and ΔT is undercooling.

3.2.2 Algorithm of growth velocity

To model the microstructural evolution of various castings, the growth of the primary phase and eutectics must be described mathematically. In this model we assume complete equiaxed solidification. Typically, for both dendritic and equiaxed grain growth, the growth velocity is calculated as a function of undercooling:

$$\text{Eq. 18} \quad \frac{dR}{dt} = \mu \cdot (\Delta T)^2$$

where μ is growth coefficient, which depends on the type of equiaxed grain described and on their assumptions. The growth coefficient is different for primary and eutectic grains.

The growth coefficient for the primary dendritic grain growth can be calculated with the Nastac-Stefanescu (N-S) model⁶, that is:

$$\text{Eq. 19} \quad \mu = \frac{2\sigma^*}{\Gamma} \left[\frac{\bar{m}_L(\bar{k}-1)C_L^*}{D_L} + \frac{\rho L}{\lambda_L} \right] \quad \text{and} \quad C_L^* = C_o \left[1 - \frac{(1-\bar{k})f_s}{1-3[\bar{k}I_s + I_L]} \right]^{-1}$$

where C_L^* is the liquid concentration at the solid-liquid interface, σ^* is a stability constant of the order of $(2\pi)^2$, Γ is the Gibbs-Thomson coefficient, ρ is the density, L is the latent heat of fusion, λ_L is the thermal conductivity of the liquid, and f_s is the fraction solid. The interdendritic liquid is assumed to be well mixed ($D_L = \infty$). I_s and I_L are calculable variables, and C_o is the initial concentration of alloy. The data used in the calculation of nucleation and growth of grains and other thermal physical properties of A356 and D357 alloys are given in Table 2.

Table 2 Data used in micro-modeling of alloys

D_S m^2s^{-1}	D_L m^2s^{-1}	L J kg^{-1}	ρ_S kg m^{-3}	ρ_L kg m^{-3}	λ_L $\text{W m}^{-2}\text{K}^{-1}$	C_o $\text{J kg}^{-1} \text{K}^{-1}$	Γ K m
1×10^{-11}	4.3×10^{-9}	3.39×10^5	2555	2376	100	1110	2.0×10^{-7}

The main assumption in the N-S model is that limited diffusion exists in both solid and liquid. The undercooling for the tip of the primary dendritic grain is:

$$\text{Eq. 20} \quad \Delta T = T_L(C_o) - T_b + \bar{m}_L(\langle C_L \rangle - C_o)$$

where ΔT is the total undercooling, C_o is the initial concentration of the alloy, T_b is the bulk temperature defined as the average temperature in the control volume. $\langle C_L \rangle$ is obtained by integrating the local concentration over the extra-dendritic liquid phase. $T_L(C_o)$ is the initial equilibrium liquidus temperature, which corresponds to the initial alloy concentration, C_o .

It is further assumed that the eutectic grain growth is controlled by thermal undercooling. However, kinetic undercooling should be considered for A356 and D357 alloys because they are non-faceted/faceted eutectic. This could constitute future work.

3.2.3 Tracking of grains

Grain movement occurs when equiaxed grains or broken dendrite tips exist during early solidification. The grains generated in one place can be carried to other places. This behavior significantly affects the final microstructure that determines the mechanical properties of castings. Grain movement in and out of the volume element will change the solid fraction within the element. This will affect overall solidification kinetics and thus the resulting microstructure and mechanical properties. The dynamics of volumetric grain density within a volume element are determined by heterogeneous nucleation and by advection of grains in and out of the volume element. In general, the number of grains moving in is not identical to that of grains moving out for any given volume element, as illustrated in Figure 3.

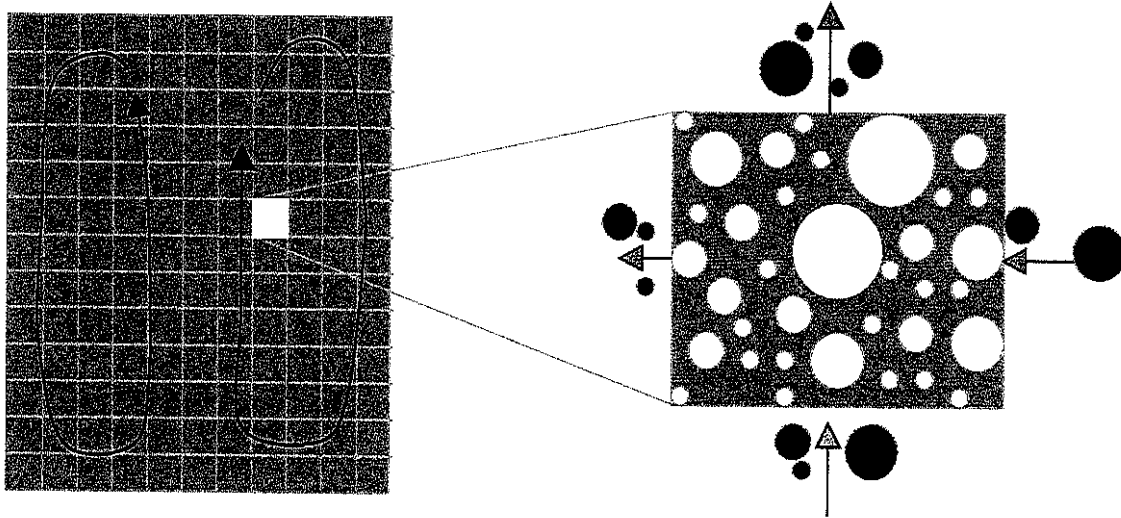


Figure 3 A schematic illustration for grain movement

The total nucleation rate in a volume element can be described by the following conservation equation:

$$\text{Eq. 21} \quad \frac{dN}{dt} = \frac{\partial N_h}{\partial t} + \nabla \cdot (V f_s N)$$

where N is the volumetric grain density, and V is the upwind velocity of the melt to the control volume, which can be obtained from the solution of the momentum equations. The total nucleation rate consists of two parts. The first part is nuclei generation through heterogeneous nucleation. It is a function of undercooling as postulated, for example by

Eq. 17. The second part describes the grain movement during the first stage of solidification (grains entering or leaving the volume element). For the 2D problem, the second term on the RHS of Eq. 21 must account for the transport relationships with four neighbor control volumes. Six surrounding control volumes should be considered for the 3D problem.

3.2.4 Distribution of grain size

In reality, the grains have different sizes in the all control volumes. Metallographic analysis demonstrates the existence of some distribution. In the current study, it is assumed that the distribution function of grain density is quadratic. The function of grain density distribution developed by Goettsch and Dantzig⁷ was selected to describe grain size distribution in each volume element, namely:

Eq. 22
$$n(r) = \frac{3N(R_{\max} - r)^2}{(R_{\max} - R_{\min})^3}$$

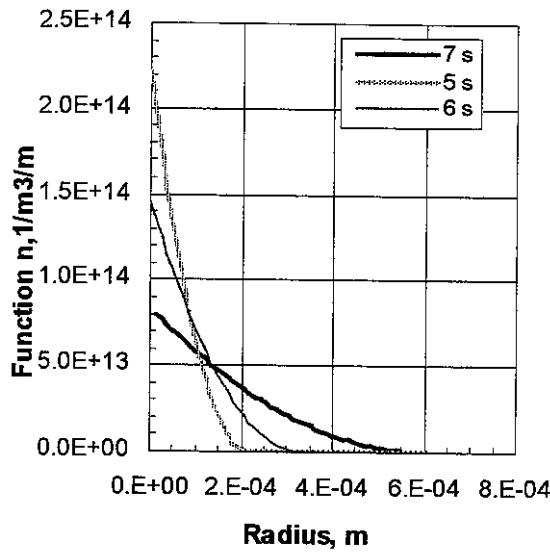


Figure 4 Variation of distribution function with time

where $n(r)$ is the grain density at a radius r , and R_{\max} and R_{\min} are the maximum and minimum radii in each control volume, respectively. During nucleation, all grains are introduced at the specified minimum size in the distribution, R_{\min} . The maximum radius, R_{\max} , and total grain density increase during solidification, while the minimum radius, R_{\min} , remains constant if new nuclei are still generated. The distribution function of volumetric grain density is shifting to larger radii with increased solidification time. A typical computed result is illustrated in Figure 4. Thus, this model considers not only the movement of the fraction solid but also the dynamic contribution of individual grains through the grain distribution function. Furthermore, the primary dendrites and eutectic grains have their own R_{\max} , and R_{\min} in each control volume, respectively.

Note that in our model grain movement was considered. Then, R_{\max} , R_{\min} and the dynamic distribution of grain density within each control volume are not dependent only on its

temperature. Furthermore, the primary dendrites and eutectic grains have their own R_{max} , and R_{min} in each control volume, respectively.

To precisely evaluate R_{max} , and R_{min} in each control volume a number of rules of grain movement have been developed by the authors⁸. The major rules are:

1. The total grain density is the algebraic sum of heterogeneously nucleated grains and of grains advected from the neighboring cells.
2. The contribution is positive when fluid brings grains into the volume element and negative when grains are moved out.
3. Every volume element is characterized by its own N , R_{max} and R_{min} .
4. If incoming grains have a higher maximum radius, R'_{max} , R'_{max} becomes the new maximum radius in the current volume element. Otherwise, the maximum radius remains unchanged.
5. The same rule applies for the minimum radius, unless nucleation continues in the volume element. In this case, R_{min} is that of the nucleus.
6. The time step must be selected such as to allow grains to move only over the distance of one control volume during the time step.

The volume fraction of the solidified spherical grains is readily computed from the distribution as

$$\text{Eq. 23} \quad g_s = \frac{\pi N}{15} (R_{max}^3 + 3R_{max}^2 R_{min} + 6R_{max} R_{min}^2 + 10R_{min}^3)$$

The final expression of the solidification rate is:

$$\text{Eq. 24} \quad \frac{dg_s}{dt} = (\Gamma \frac{dN}{dt} + \Theta \frac{dR_{max}}{dt} + \Phi \frac{dR_{min}}{dt}) (1 - g_s)^{g_s}$$

Where Γ , Θ , and Φ are obtained from the following expressions:

$$\begin{aligned} \Gamma &= \frac{\pi}{15} (R_{max}^3 + 3R_{max}^2 R_{min} + 6R_{max} R_{min}^2 + 10R_{min}^3) \\ \Theta &= \frac{\pi N}{15} (3R_{max}^2 + 6R_{max} R_{min} + 6R_{min}^2) \\ \Phi &= \frac{\pi N}{15} (3R_{max}^2 + 12R_{max} R_{min} + 30R_{min}^2) \end{aligned}$$

Originally, it is assumed that grains have a spherical shape throughout the entire growth process. This assumption is not valid at large solid fraction when grains impinge on one another. Based on previous work^{6,7}, the impingement factor $(1 - g_s)^{g_s}$ was introduced in Eq. 24 to account for the effective surface interfacial area between the solid equiaxed dendritic grains and the liquid phase. The classic Avrami correction factor $(1 - g_s)$ was

derived for the case of spherical grains, for which coherency occurs rather late, e.g., at 0.74 fraction of solid. However, since dendrites are not spheres, their coherency will appear considerably faster than that of spherical grains, i.e., when their dendrite envelopes collide. Accordingly, the impingement factor was modified to describe the onset of impingement at an earlier stage.

Unlike the Avrami correction factor, which must be used only during the late stages of solidification, the impingement factor in Eq. 24 is used from the beginning to the end of solidification. It becomes important when $g_s \geq 0.5$.

3.2.5 Competitive growth and non-equilibrium solidification

From the equilibrium binary phase diagram, when the bulk temperature at any location in the casting is below the eutectic temperature, nucleation and growth of the eutectic phase begin. During the eutectic transformation, the temperature and the composition are constant, and the primary dendrites stop growing once eutectic temperature is reached. However, the alloy system of consideration is not a simple binary alloy and its solidification does not follow equilibrium. A356 and D357 alloys belong to a multi-component alloy system, which have 5 to 7 elements, as shown in Table 4. The eutectic reaction does not take place at a constant temperature or at a constant composition. Rather, it occurs in a temperature interval and in a composition range. The eutectic transformation occurs over a temperature interval and with variable concentration, which depends on the cooling rate, diffusivity, etc. Growth competition between eutectic and dendritic phases appears below the beginning of eutectic transformation and continues to the end of solidification. In other words, during the eutectic transformation two different phases coexist, and grow competitively, dendritic and eutectic grains.

A typically temporal computed solid fraction is shown in Figure 5. The computed results of solid fraction demonstrate that the dendrite fraction increases about 10% from the start to the end of eutectic solidification. It is also seen that the proposed model reveals that the eutectic fraction increases faster than the dendrites during the eutectic transformation.

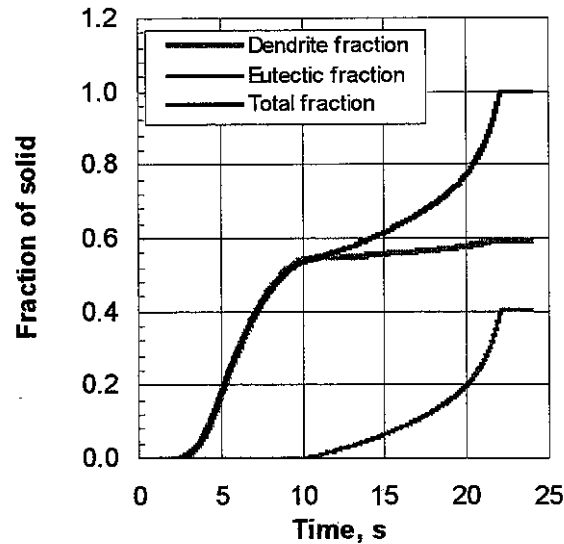


Figure 5. Temporal solid fraction in a certain sample.

Note that the criterion to start the eutectic transformation of the non-equilibrium transformation is not eutectic temperature alone. Temperature and composition must both be considered. For any volume elements in castings the eutectic reaction begins when the two following conditions are satisfied:

$$T < T_E \quad C_L^* \geq C_E$$

where T is a bulk temperature, and T_E is the eutectic temperature from the equilibrium phase diagram, which will be discussed in the section of thermophysical properties. C_L^* is the liquid concentration at the solid-liquid interface, and C_E is the beginning composition of the eutectic reaction, which is increased to a certain extent due to non-equilibrium solidification.

3.2.6 Segregation models

In this work, we consider two kinds of the segregation. The first one is micro-segregation. The second one is macrosegregation. Assessment of segregation occurring in solidifying alloys is also important because it affects mechanical properties. Macrosegregation relates directly to the micro-segregation. We will discuss micro-segregation first.

Micro-segregation comes from the redistribution of elements during the solidification of casting alloys. A summary of the major assumptions used in some analytical micro-segregation models is given in Table 3. The basic equations for those models are given in ref. ⁹. It can be seen that the micro-segregation models can be divided into two groups. The first group is composed of the models sharing the common assumption that within a small volume element, the solute concentration in the liquid is uniform, *i.e.*, the solute diffusion coefficient in the liquid phase is very high. The solute concentration in the liquid follows the liquidus line and is determined by the current temperature in the alloy volume. In all these models the solid fraction evolved depends on temperature but is not influenced by the cooling rate. The models from the second group assume limited solute diffusion in the liquid phase. This leads to the development of a concentration gradient in front of the solid/liquid interface.

Table 3 Major assumptions used in analytical microsegregation models

Model	Geometry	Solid diffusion	Liquid Diffusion	Partition coefficient	Growth	Coarsening
Lever rule	No restriction	Complete	Complete	Variable	No restriction	No
Scheil	No restriction	No	Complete	Constant	No restriction	No
Brody/Flemings	No restriction	Incomplete	Complete	Constant	No restriction	No
Clyne/Kurz	No restriction	Spline fit	Complete	Constant	No restriction	No
Ohnaka	Linear, columnar	Quadratic eq.	Complete	Constant	Linear, parabolic	No
Sarreal/Abbaschian	No restriction	Limited	Complete	Constant	No restriction	No
Kobayashi	Columnar	Limited	Complete	Constant	Linear	No
Nastac/Stefanescu	Plate, columnar, equiaxed	Limited	Limited	Variable	No restriction	Yes

Under common casting conditions non-equilibrium solidification occurs. The redistribution of solute at the microscopic level is controlled by diffusional transport. Since the local solidification conditions determine the diffusion time, the degree of micro-segregation

depends on solidification. Thus, the solute diffusion in solid and liquid is limited. The Nastac-Stefanescu (N-S) model was chosen in the current program because it allows for limited solute redistribution in the primary phase (back diffusion) and liquid. Based upon the N-S model ⁶, the intrinsic volume average concentration $\langle C_L \rangle$ is obtained by integrating the local concentration over the extradendritic liquid phase. The intrinsic volume average within a volume element can be calculated with the following formula:

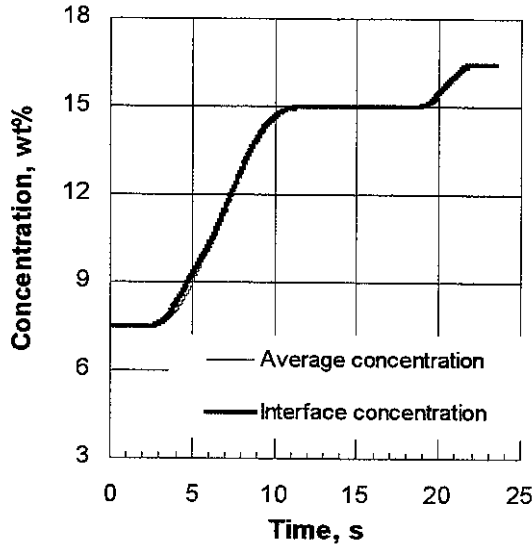


Figure 6 Variation of interface concentration C_L^* and intrinsic volume average concentration $\langle C_L \rangle$ during solidification

$$\text{Eq. 25} \quad \langle C_L \rangle^L = C_L^* + \Omega \cdot (C_0 - C_L^*)$$

where Ω is a calculable variable from ref. ⁶, and C_L^* is the concentration at the solid/liquid interface, as expressed in Eq. 19. For instance, the dynamic variation of average concentration, $\langle C_L \rangle$ with solidification time is shown in Figure 6. It is seen that the tendency of C_L^* and $\langle C_L \rangle$ is the same. However, concentration gradients exist at times. C_L^* and $\langle C_L \rangle$ will approach the same value later during solidification.

In addition to microscopic solute redistribution, fluid flow and transport of solid fragments occurring during solidification generates compositional non-uniformity at the macroscopic level. The resulting chemical anisotropy is called macrosegregation. This macrosegregation may result in a significant variation of the physical and chemical properties throughout the entire casting. It is well known that elimination of macrosegregation is extremely difficult. For alloys with primary dendrites and eutectic phase, the average solute concentration in the solidified solid within each volume element can be calculated from:

$$\text{Eq. 26} \quad \overline{C_s} = \int_0^{f_s(T_E)} C_s^* df_s + \int_{f_s(T_E)}^1 C_s^* df_s^P + \int_{f_s(T_E)}^1 C_L^* df_s^E$$

where T_E is the eutectic temperature, f_s^P is the mass fraction of solid dendrites, f_s^E is the mass fraction of eutectic phase, C_s^* is solute concentration of solid at the interface, and C_L^* is solute concentration of liquid at the interface.

3.3 Coupling of macro- and micro-modeling

3.3.1 Coupling problems

To model microstructural evolution during solidification the macro-transport and micro-transport must be solved simultaneously. The coupling between macro-transport and micro-transport is through the source term in the energy equation, which must carry out the solidification kinetics (micro-transport). Because the heat flux obtained from nucleation and growth of grains is highly nonlinear, it may result in the divergence of the temperature field, or bring about oscillating behavior of the cooling curves. Another problem is accuracy, which is very important to predict microstructural evolution, especially for the model with the grain tracking.

Based on an existing study¹⁰, the Latent Heat Method (LHM) was chosen to deal with the release of latent heat through nucleation and growth during solidification. The LHM can give the most accurate results in the macro- and micro-transport codes because it uses the same time step for both of them. The drawback of this method is a relatively longer computational time resulting from the requirement for a small time step.

3.3.2 Numerical procedure

A fully implicit control-volume-based finite difference method was used to discretize the strongly coupled transport equations summarized in Eq. 16. The Semi-Implicit Method for Pressure-Linked Equations Revised (SIMPLER) was employed to handle the pressure-velocity coupling for the momentum equations. The upwind scheme is used for the convection terms. A staggered grid is applied to discretize the momentum equations. A detailed discussion of the solution algorithm along with its single-phase version can be found in ref. ¹¹. Since the continuum approach was chosen for macro-modeling, all transport equations are equally applicable to solid, mushy and liquid zones. Therefore they can be solved using a fixed-grid, single-domain numerical solution procedure.

The velocity field was calculated from the momentum and continuity equations at each time-step using the updated properties of each control volume. Within each iteration, the micro-model was called to calculate nucleation and growth for each control volume, and fraction of solid and heat flux were obtained. These data were fed back to solve the energy equation to obtain the temperature field. In the next time step, the properties of each control volume were updated and the velocity field was solved again. All the above steps were repeated until all the control volumes solidified. The iterative numerical procedure is represented schematically in Figure 7.

In the energy equation, the variation of solid fraction, $\Delta\{f_s\}$, between t and $t+\Delta t$ at all nodes is computed based on the micro-transport model of solidification, including the contributions of heterogeneous nucleation, grain movement, and grain growth. The variation, $\Delta\{T\}$ can be derived implicitly from macro-transport equations, while the

variation $\Delta\{f_s\}$ is given explicitly at each node, at time t , in order to compute the new temperature field $T(t+\Delta t)$.

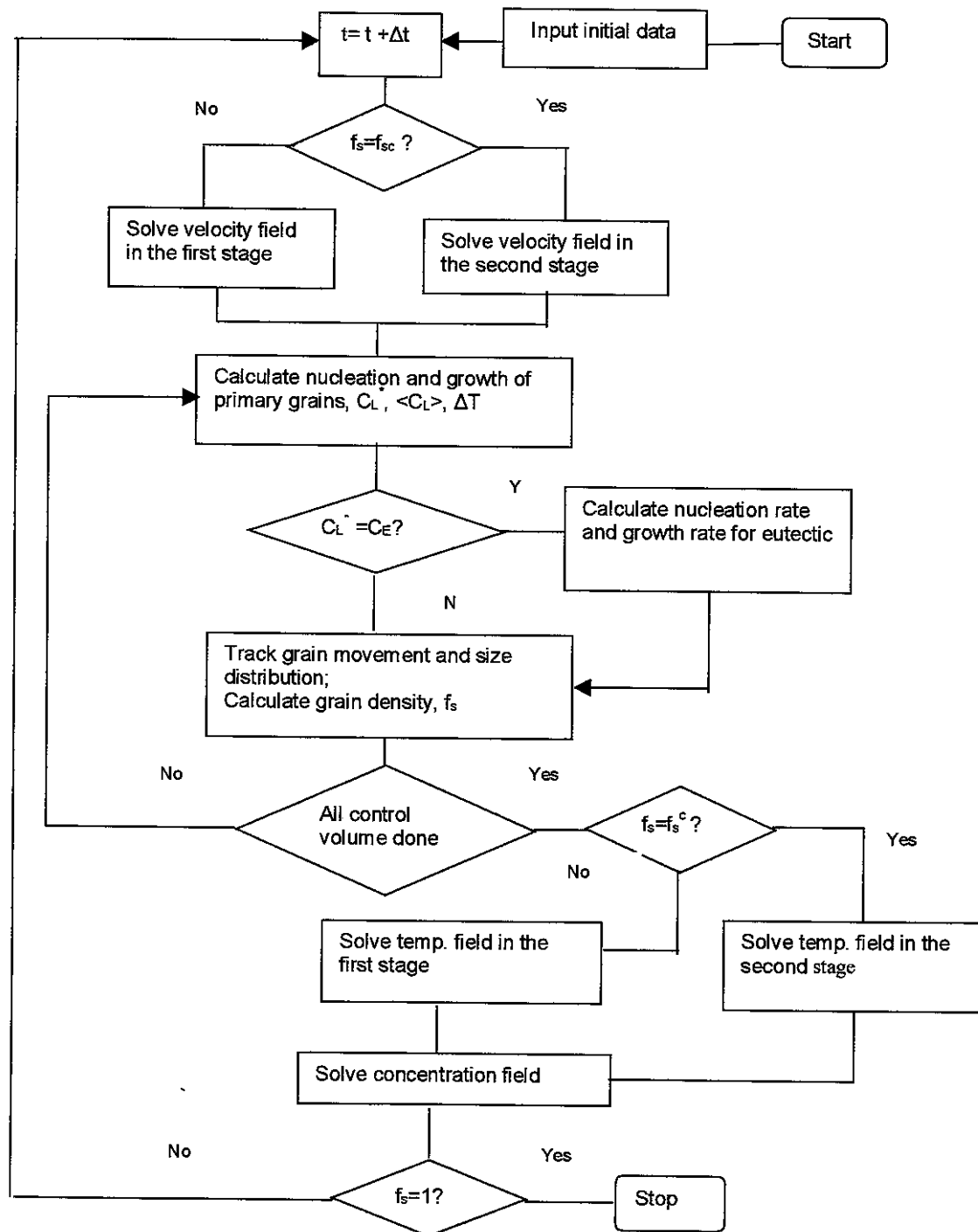


Figure 7 Flow chart of numerical procedure

4. Calculation of the thermophysical properties

The micro-transport model requires a number of material parameters that are not readily available. To determine the grain growth velocity, we need to know the liquidus temperature, T_L , which is a function of the alloy composition. In addition we also need the slope of liquidus line, m_L , and the partition coefficient, k , to calculate the growth coefficient. While finding the values of these four parameters is trivial for binary alloys, the problem becomes much more complicated for multi-component alloys. It is thus necessary to develop the data base for the alloys of interest. In the following section, we present an analysis of the possible approaches to evaluate these parameters for the aluminum-based alloys, that is, A356 and D357. The complete chemistry of the alloys of interest in this research is given in Table 4.

Table 4 Chemical compositions of alloys A356 and D357

Alloy	Elements, wt%								
	Al	Si	Mg	Fe	Mn	Cu	Zn	Ti	Other
A356	91.7	7.0	0.35	0.20	0.10	0.20	0.10	0.20	0.15
D357	91.83	7.0	0.57	0.20	0.10	-	-	0.15	0.15

4.1 Possible approaches

The following methods of evaluating selected solidification parameters will be discussed: binary alloy systems, multicomponent alloy, and pseudo-binary systems.

4.1.1 Binary alloy system

For binary alloys, the liquidus temperature (T_L), the eutectic temperature (T_E), the liquidus slope (m_L), and the partition coefficient, (k), can be obtained directly from the phase diagram. For the two alloys of interest the values of these parameters are given in Table 5. Note that m_L and k are given as average values over the indicated interval.

Table 5 Material parameters for binary alloys (units are wt%)

Alloy	Binary	T_L °C	T_E °C	m_L	k
A356 and D357	Al-Si (7 to 12.6% Al)	662.2-6.913· $\langle C_L \rangle$	577	-7.4	0.13
	Al-Fe (<1.8% Fe)		652	-4.69	0.01
	Al-Cu (0.2% Cu)	660	548.2	-3.43	0.17
	Al-Mn (<1.25% Mn)		658	-1.96	0.62
	Al-Mg (<38.5% Mg)		450	-5.84	0.47
	Al-Zn (<20 % Zn)		381	-2.22	0.52
	Al-Ti (<0.18% Ti)			25.27	6.9

In a first approximation, both aluminum alloys can be considered binary Al-Si alloys. This means that the effect of the other elements on the equilibrium temperature and on the slope and partition coefficient is negligible.

4.1.2 Multi-component alloy

When dealing with multi-component alloys the solute transport equations must be solved for each element. This requires knowledge of the influence of the elements on the equilibrium temperatures. The slope and partition coefficient must be known for each element. Calculations become more complicated.

Assuming weak or no interaction between the elements the liquidus temperature can be calculated with the following equation:

$$\text{Eq. 27} \quad T_L = T_M + \sum_i^n m_L^i \langle C_L^i \rangle$$

where T_M is the melting point of the pure metal, n is the total number of elements, and $\langle C_L^i \rangle$ is the average liquid composition in the volume element. The initial liquidus temperature can be obtained from this equation by choosing $C_L^i = C_o^i$, where C_o^i is the initial liquid composition. Similarly, the solidus temperature can be computed by setting $C_L^i = C_f^i$, where C_f^i is the final liquid composition. The data in Table 4 are used.

For multicomponent alloys the liquidus slope for an element i (K/wt%) can be estimated with Vant'Hoff relationship:

$$\text{Eq. 28} \quad m_L^i = \frac{-RT_M^2(1 - k_i)}{100 \Delta H_M M_i}$$

where R is the gas constant (8.3144 J/mole/K), T_M is the melting point of the pure metal, k_i is the partition coefficient, ΔH_M is the enthalpy of liquid/solid transformation (J/g) and M_i is the atomic weight of element i (g/mole). However, to perform this calculation we need to know the partition coefficient. This parameter can be obtained from experiments (quenching or directional solidification) carried on the multi-component alloy.

Another approach to calculate the parameters of interest is through the use of thermodynamics software. The CALPHAD method¹² was used to obtain the data. The CALPHAD method employs free energy of phases whose functional dependence on temperature and concentration approximates simple physical models for the atomic interactions of each phase. The concentrations of the solids in equilibrium with a given liquid concentration at a given temperature are obtained by equating the chemical potentials of each component in the coexisting phases according to standard thermodynamic principles. This approach has been incorporated in the commercial code ProCAST as the subroutines *LEVER* and *SLOPE*.

An example of the output of *SLOPE* is provided in Table 5. From this output, we can calculate the slope, m_i , and the partition coefficient k_i , for each element over the temperature interval of interest.

Table 5 Example of output of *SLOPE* for alloy A356 at 600 °C. The units of concentration are wt% and of the liquidus slope °C/wt%.

	Si	Fe	Cu	Mn	Mg	Ti	Zn
C_L	9.23	0.27	0.26	0.12	0.46	0.13	0.12
C_S	1.09	0.003	0.036	0.039	0.066	0.375	0.059
m_{SI}	-7.13	-1.83	-3.63	-1.32	-2.19	1.09	-2.29
k_{SI}	0.118	0.011	0.138	0.325	0.143	2.88	0.492

For example, the slopes of the liquidus line for Si as a function of temperature for the A356 and D357 alloys were calculated to be:

Eq. 29 for A356: $m_{Si} = -17.95 + 0.018 \cdot T$

for D357: $m_{Si} = -18.16 + 0.0186 \cdot T$

A summary of the calculation for the partition coefficient for both alloys is given in Figure 8.

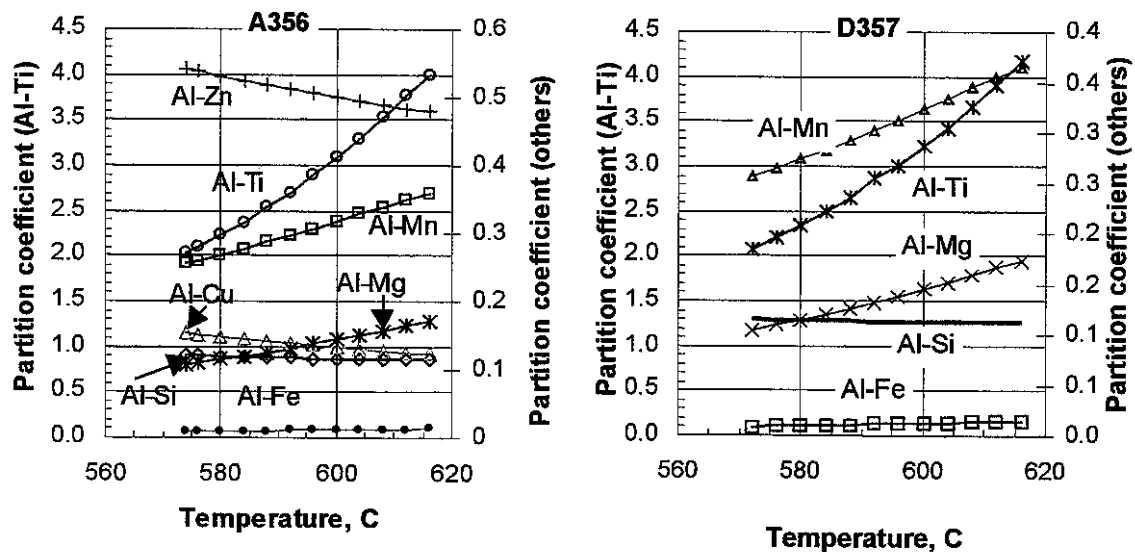


Figure 8 Temperature variation of partition coefficient in multi-component alloys

In addition, the liquidus temperature as a function of composition can also be calculated by using the least squares method. The following results were obtained:

Eq. 30 for A356:
$$T_L = 660.45 - 7.345\langle Si_L \rangle - 124.94\langle Cu_L \rangle - 216.17\langle Mn_L \rangle + 69.07\langle Mg_L \rangle + 29.22\langle Ti_L \rangle + 27.93\langle Zn_L \rangle$$

$$\begin{aligned} \text{for D357: } T_L &= 660.45 - 7.124\langle Si_L \rangle + 120.04\langle Fe_L \rangle + 363.14\langle Mn_L \rangle \\ &\quad - 99.78\langle Mg_L \rangle + 23.24\langle Ti_L \rangle \end{aligned}$$

It is seen that to calculate the liquidus temperatures we need to know the concentration of each element in the liquid. If these equations are used in the micro-model, diffusion equations must be solved for each element. This is a complicated and time-consuming procedure.

The beginning temperatures of the eutectic transformation for the two alloys were calculated to be:

$$\text{for A356: } T_E = 572 \text{ } ^\circ\text{C}$$

$$\text{for D357: } T_E = 570 \text{ } ^\circ\text{C}$$

Note that both are lower than the eutectic temperature (577°C) in the Al-Si binary system.

4.1.3 Pseudo-binary systems

As discussed above, when calculating the solidification parameters of interest by using thermodynamic calculations for multi-component alloys one needs to solve the mass transport equation for each species. For these alloys, this means five to seven different elements and thus equations.

To avoid excessive computation, a simpler approach is to treat the multicomponent alloy as a pseudo-binary alloy. The liquidus temperature of the pseudo-binary alloy can be obtained as:

$$\text{Eq. 31} \quad T_L = T_M + \bar{m}_L \cdot \bar{C}_L \quad \text{with} \quad \bar{C}_L = \sum_{i=1}^n C_L^i$$

where \bar{C}_L is the equivalent liquid concentration. This equation can be used to calculate the initial liquidus temperature and the final solidification temperature. The equivalent liquidus slope and the equivalent partition coefficient of the pseudo-binary alloy can be calculated with:

$$\text{Eq. 32} \quad \bar{m}_L = \frac{\sum_{i=1}^n (m_L^i C_L^i)}{\bar{C}_L} \quad \text{and} \quad \bar{k} = \frac{\sum_{i=1}^n (m_L^i C_L^i k^i)}{\sum_{i=1}^n (m_L^i C_L^i)}$$

Here, \bar{m}_L and \bar{k} are the equivalent slope and equivalent partition coefficient, respectively, \bar{C}_L is the sum of all the elements in the liquid, and m_L^i , C_L^i , and k_L^i are the slope, liquid composition, and partition coefficient of individual elements, respectively.

The *SLOPE* subroutine in ProCAST calculates the slope of the liquidus line and the partition coefficient for each element at successive temperatures. Then, an equivalent slope and a partition coefficient were obtained for each temperature using the equations. The variation of the equivalent liquidus slopes of A356 and D357 is shown in Figure 9,

and the variation of the equivalent partition coefficient is demonstrated in Figure 10. The regression equations were fitted through the m_L-T and k_L-T curves.

From Figure 9 and Figure 10, it can be seen that the liquidus slopes of two alloys are close, but the partition coefficients of two alloys are different. The partition coefficient of A356 alloy is almost constant with temperature as it is in binary alloy system, while it is temperature dependent for D357 alloy. The results indicate that the partition coefficient of multi-component alloy is more sensitive to its composition than the liquidus slope. The equivalent partition coefficient of two alloys is different mainly because of the different zinc content. This difference between two alloys will affect the microstructure evolution.

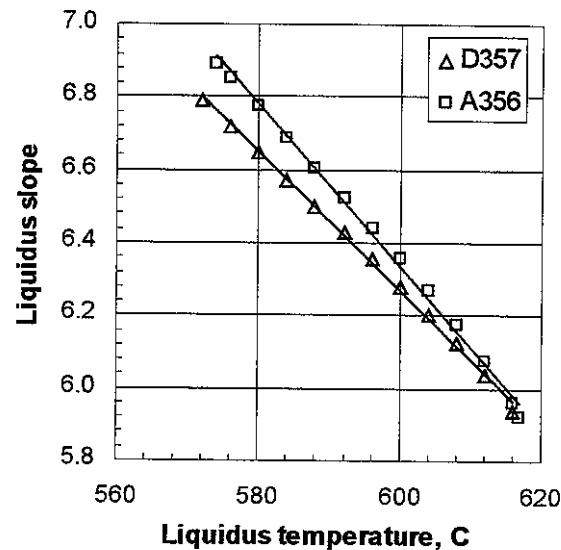


Figure 9 The variation of liquidus slope of A356 and D357 with liquidus temperature

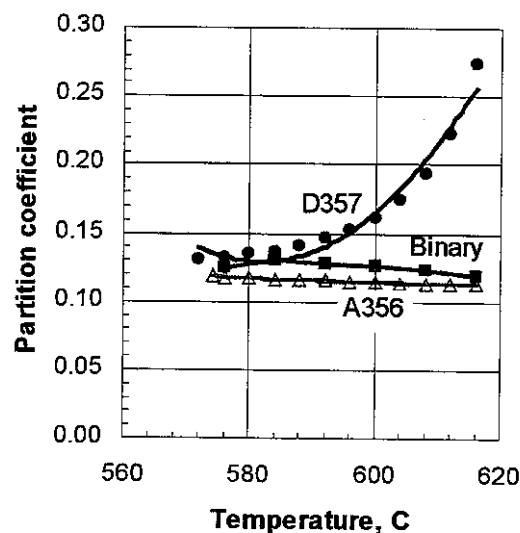


Figure 10 Comparison of partition coefficient

4.2 Comparison between various approaches

The three approaches to calculate the liquidus temperature are compared in Figure 11. It can be seen that the pseudo-binary approach generates data close to the multi-component approach for the liquidus temperature when using the appropriate equivalent liquid concentration. Note that if the equivalent liquid concentration at a given temperature is calculated through a simple sum of each individual element, the pseudo-binary approach still cannot give reasonable results. For example, the sum of each element concentration is 8.15 wt% at the beginning of solidification. Then, the liquidus temperature is 611.8 °C. However, based on thermodynamic calculations for A356 it should be 617.5 °C. Thus, it is necessary to devise a method to evaluate the equivalent liquid concentration for aluminum-base alloys.

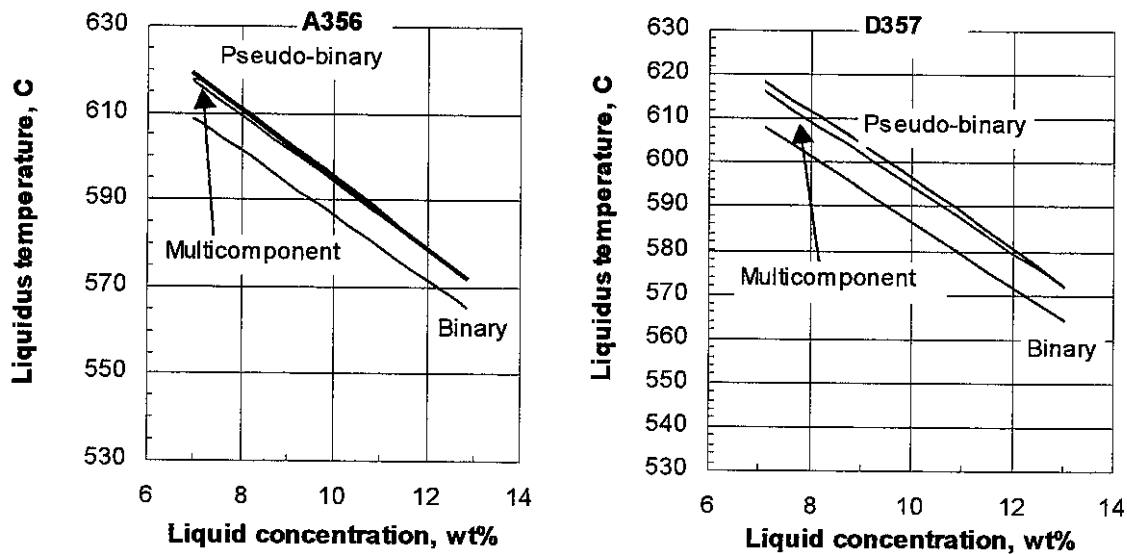


Figure 11 Liquidus temperature of A356 and D357 against liquid concentration

The equivalent liquid concentration of Si can be estimated with a weighted sum, that is:

Eq. 33

$$\langle Si \rangle^E = \langle Si \rangle + \sum_{i=1}^n \alpha_i \cdot \langle C_L^i \rangle$$

where α_i is weighted factor that reflects the interaction between elements, n is the number of elements, and $\langle C_L^i \rangle$ is the average liquid concentration of element i in the volume element. From the data provided by ProCast, the average liquid concentration of each element is known at a given temperature. The equivalent silicon content, $\langle Si \rangle^E$ for a given temperature is measured on the binary phase diagram of Al-Si. All data for A356 and D357 are shown in Table 6 and Table 7.

All weighted factors in Eq. 33 can be readily evaluated using the linear regression method. For the aluminum-base alloys of interest, we obtain:

Eq. 34 for A356 $\langle Si \rangle^E = \langle Si \rangle + 44.872\langle Fe \rangle - 80.318\langle Cu \rangle - 47.763\langle Mn \rangle + 15.365\langle Mg \rangle + 1.194\langle Ti \rangle + 61.025\langle Zn \rangle$

for D357 $\langle Si \rangle^E = \langle Si \rangle - 113.839\langle Fe \rangle - 189.378\langle Mn \rangle + 72.797\langle Mg \rangle - 0.0766\langle Ti \rangle$

Table 6 Liquid concentration and equivalent Si for A356

$T_L(^{\circ}C)$	$\langle Si \rangle$	$\langle Fe \rangle$	$\langle Cu \rangle$	$\langle Mn \rangle$	$\langle Mg \rangle$	$\langle Ti \rangle$	$\langle Zn \rangle$	$\langle Si \rangle^E$
616	7.153	0.205	0.204	0.102	0.357	0.186	0.101	7.0
610	7.911	0.229	0.226	0.109	0.393	0.149	0.107	7.5
608	8.173	0.238	0.233	0.112	0.405	0.142	0.109	7.8
604	8.704	0.256	0.248	0.118	0.431	0.133	0.113	8.5
600	9.237	0.274	0.262	0.123	0.457	0.127	0.116	9.0
588	10.824	0.331	0.305	0.140	0.539	0.124	0.124	10.6
584	11.345	0.351	0.318	0.146	0.567	0.126	0.126	11.0
580	11.862	0.371	0.331	0.152	0.596	0.128	0.128	11.6
576	12.373	0.391	0.344	0.158	0.625	0.130	0.130	12.6

Table 7 Liquid concentration and equivalent Si for D357 alloy

$T_L(^{\circ}C)$	$\langle Si \rangle$	$\langle Fe \rangle$	$\langle Mn \rangle$	$\langle Mg \rangle$	$\langle Ti \rangle$	$\langle Si \rangle^E$
616	7.109	0.204	0.101	0.578	0.142	7.0
610	7.897	0.229	0.109	0.638	0.111	7.5
608	8.169	0.238	0.112	0.659	0.105	7.8
604	8.716	0.256	0.117	0.702	0.098	8.5
600	9.265	0.275	0.123	0.745	0.093	9.0
588	10.895	0.333	0.140	0.880	0.090	10.6
584	11.429	0.353	0.146	0.926	0.091	11.0
580	11.958	0.373	0.152	0.974	0.092	11.6
576	12.482	0.393	0.157	1.022	0.094	12.6

It is seen that, to calculate the equivalent concentration of silicon in the liquid, we must know the liquid concentration of each element. As with the liquidus temperature of multi-component alloys, if these formulas are used in the micro-model, diffusion equations must be solved for each element. This is a complicated and time-consuming procedure.

However, it is noticed from Table 6 and Table 7 that at a given temperature the equivalent concentrations of Si measured on Al-Si phase diagram are close to the liquid concentration of $\langle Si \rangle$ obtained from the thermodynamic calculation of the multi-component. In a first approximation, in the pseudo-binary method we will only use the liquid concentration of $\langle Si \rangle$ as the equivalent concentration of alloys, which is to be computed using mass transport equation.

Based on the results in Table 6 and Table 7, a combined approach, called an equivalent pseudo-binary, was proposed. In this approach, the phase diagram of the binary system was used to calculate the liquidus temperature, but the liquidus slope was not taken from the binary phase diagram. The effect of all elements on the liquidus temperature was considered through the liquidus slope. To calculate the liquidus temperature by the equivalent pseudo-binary alloy, the equivalent slope resulting from the effect of all elements, and the average Si content in the liquid were used as follows:

Eq. 35
$$T_L = T_M + \overline{m}_L \cdot \langle Si \rangle$$

where T_M is the melting temperature of pure aluminum, and $\langle Si \rangle$ is the liquid concentration of Si .

4.3 Summary of relationships for A356 and D357 alloys

In summary, the following equations are used to evaluate the liquidus temperature and the liquidus slope:

Eq. 36
$$T_L = 660.45 + m_L \cdot \langle Si \rangle$$

Eq. 37
$$m_L = \begin{cases} 0.0221T - 19.61 & \text{for A356} \\ 0.0189T - 17.64 & \text{for D357} \end{cases}$$

Eq. 38
$$k = \begin{cases} 0.115 & \text{for A356} \\ 1.09248 \times 10^{-4} \cdot T^2 - 1.27122 \times 10^{-1} \cdot T + 37.1092 & \text{for D357} \end{cases}$$

5. Model verification

5.1 Design of test sample and its boundary conditions

A rectangular sample 20 mm high and 10 mm wide was selected for general verification of the proposed macro-micro model. It is assumed that the aluminum metal fills the cavity instantaneously. The heat is extracted from the bottom and the two sidewalls. An insulated boundary was set on the top surface. No-slip and no-penetration conditions were set on the three boundaries of heat extraction. Figure 12 shows the physical model and the calculation conditions. The casting was discretized with a 20 x10 grid.

5.2 Implementation on A356 and D357

For the A356 alloy, the initial liquidus temperature is 617.5 °C, and the eutectic temperature is 572 °C. Using the proposed model and all parameters obtained for the pseudo-binary alloys, the calculated cooling curve and the temporal evolution of the solid fraction at position B in Figure 12 (12 mm from the bottom) are shown in Figure 13. Since a fully modified melt is assumed, a large undercooling is apparent. The cooling curve exhibits no recalescence and the undercooling remains very large during the eutectic plateau. This feature agrees well with experimental findings^{13,14,15}.

The cooling curves at different cooling rates (different positions at top, center and bottom of the sample) are shown in Figure 14. No discernible recalescence during the eutectic transformation is apparent.

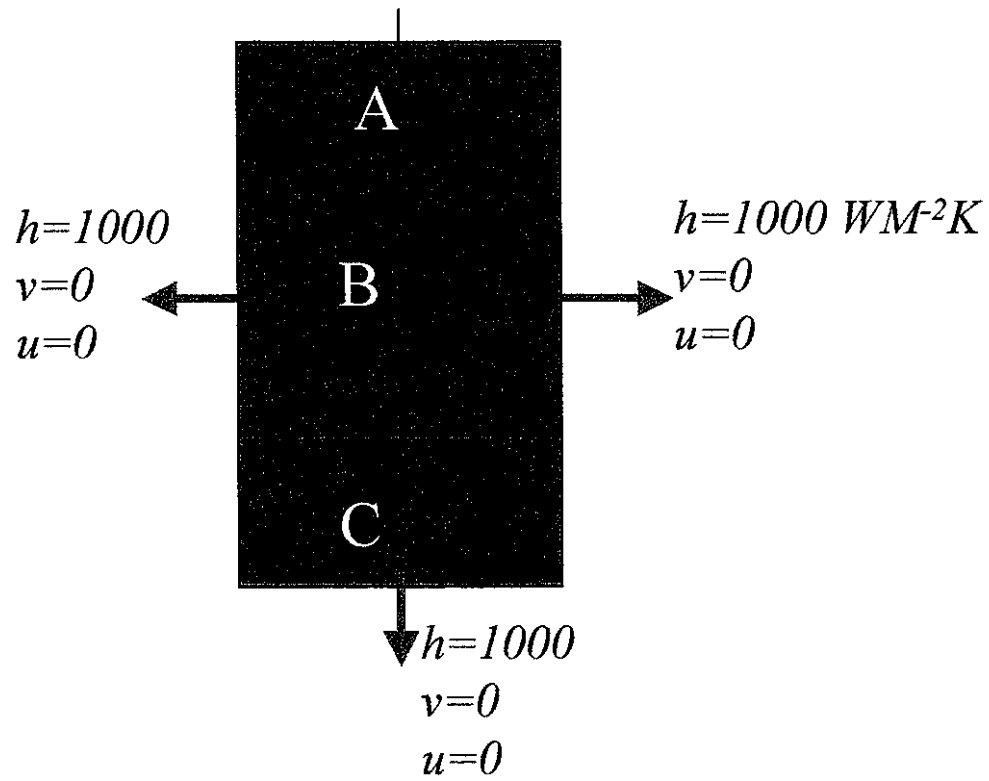


Figure 12 Testing sample and boundary conditions

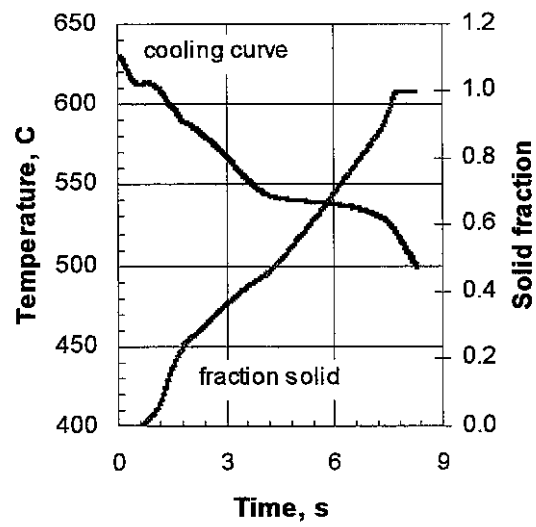


Figure 13 Calculate cooling curve and fraction of solid at Point B

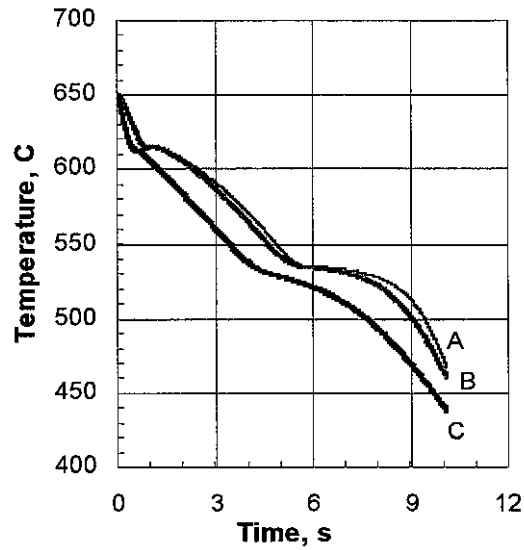


Figure 14 Cooling curves at different locations of the sample

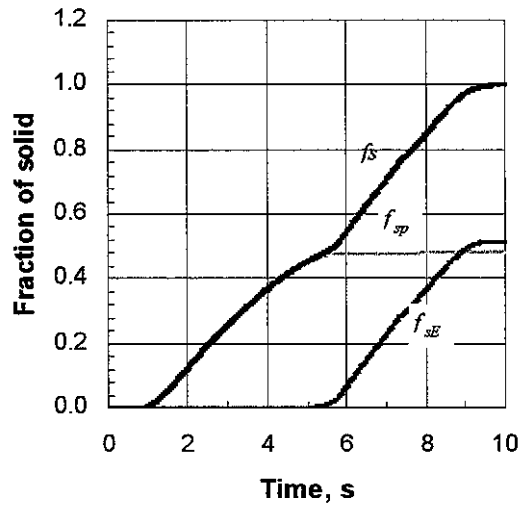


Figure 15 Evolution of solid fraction during solidification

Figure 15 shows the evolution of solid fraction of the dendrites and the eutectic at position A. It illustrates the competitive growth between primary and eutectic phases during solidification. The final distribution of the amount (fraction) of eutectic is presented in Figure 16. Less eutectic (more dendrites) is formed near the bottom chill and the two sidewalls where the cooling rate is higher. In these regions, the amount of eutectic is far from that predicted from equilibrium solidification. In a position with a relatively low cooling rate, such as in the center and near the insulated interface, the amount of eutectic is closer to that calculated from the phase diagram. This result shows that the local cooling rate will induce a different distribution of the phases during non-equilibrium solidification than that predicted from equilibrium solidification (phase diagram).

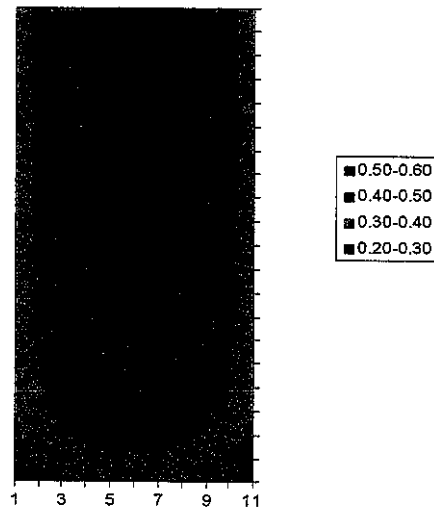


Figure 16 Distribution of the eutectic fraction for A356 alloy

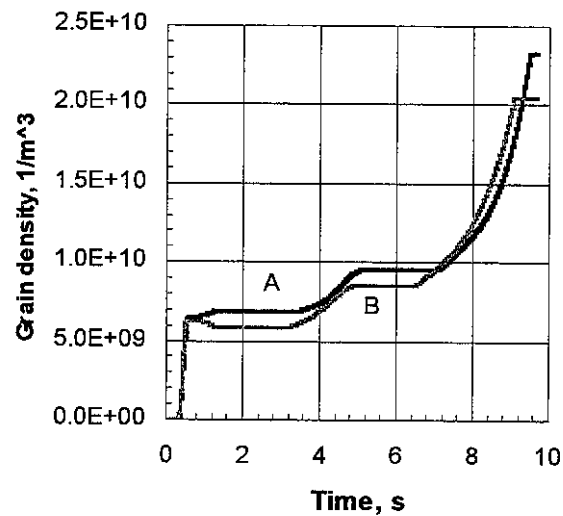


Figure 17 Variation of total volumetric grain density at position A and B

Figure 17 shows the change of the total volumetric grain density at position A and B during solidification. It can be seen that because of the grain movement, the grain density within the control volume under consideration may decrease or increase before the start of eutectic solidification. At position A, the number of grains moving in is greater than that of grains moving out within the control volume, thus the grain density increases before the start of eutectic transformation. However, the grain density decreases at position B in the same period because of the same reason. It demonstrates that the model correctly describes the balance of volumetric grain density across the casting. Furthermore, it suggests that the grain movement considerably affects the distribution of grain density.

Figure 18 represents the final distribution of the dendrite fraction for the D357 alloy. A similar distribution was computed for the A356. The amount of dendrites is strongly dependent on the cooling rate, and their distribution is also affected by the flow.

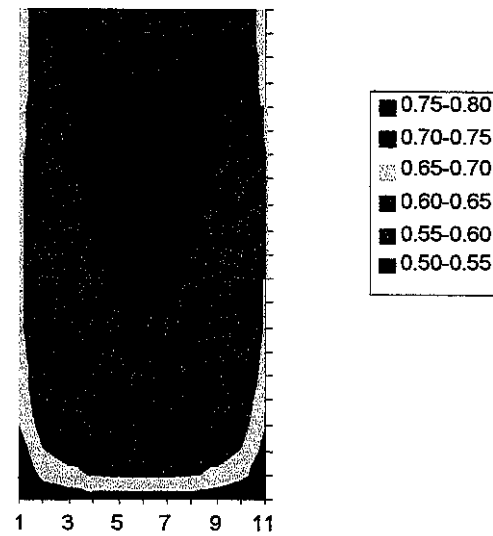
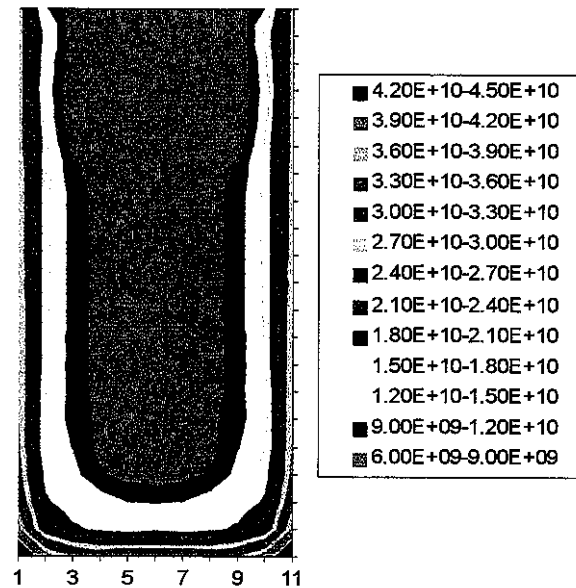
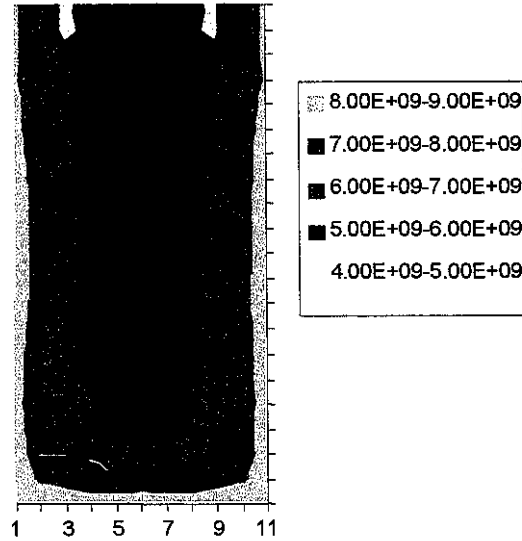


Figure 18 Final distribution of dendrite fraction of D357 alloy



(a) Dendrites



(b) Eutectic

Figure 19 Grain densities for dendrites and eutectic phase for D357 alloy

The distributions of the volumetric grain densities of dendrites and eutectic for the D357 alloy are plotted in Figure 19. Because the grains in each control volume can be moved from one location to another by advection before coherency occurs, the flow caused by the natural convection, shrinkage and grain movement has even more influence on the dendrite distribution than the eutectic grain distribution.

The distribution of the equiaxed eutectic grain having the largest size in each volume element is shown in Figure 20. It can be seen that the distribution depends not only on the cooling rate, but also on liquid flow.

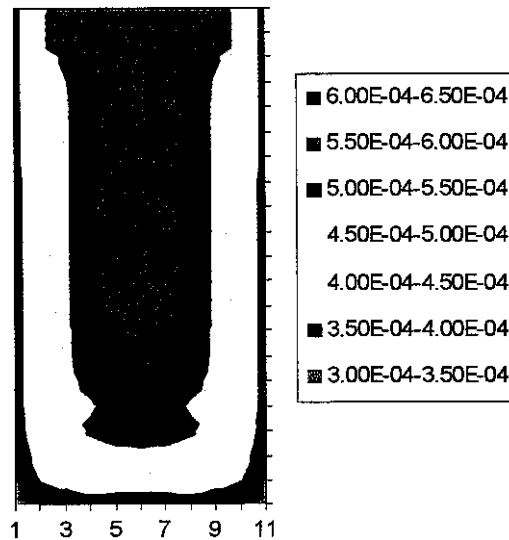


Figure 20 The largest radius of eutectic grains

5.3 Case study

In order to demonstrate the effect of grain movement on the solidification microstructure, three cases were simulated:

- a) no solid movement during solidification;
- b) solid movement but no grain tracking;
- c) solid movement with grain tracking.

The cooling curves at position B in Figure 12 are plotted in Figure 21 for the three cases. Note the decrease in primary undercooling when flow is included in calculation.

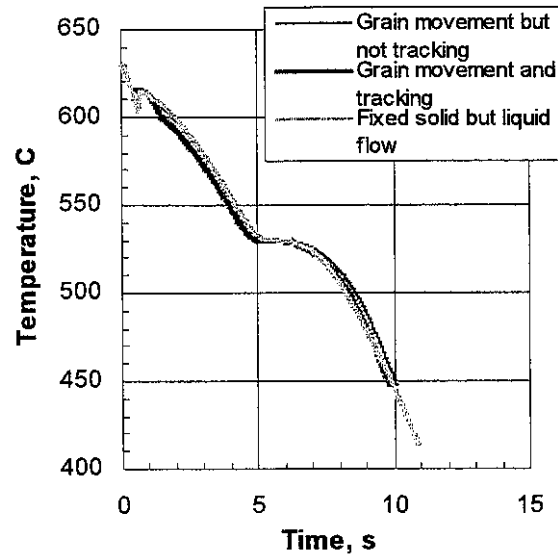


Figure 21 Cooling curves under different cases

The final distribution of fraction of equiaxed dendrites for alloy A356 is shown in Figure 22 for three different calculation conditions. Significant differences are observed. Indeed, when comparing the case for no solid movement with that where solid movement but no grain tracking was included in calculation, it is seen that the bottom of the ingot has a much larger fraction of dendrites. In fact the structure is almost fully dendritic at the bottom when solid movement was ignored (Figure 22a). It is also seen that when grain tracking was used (Figure 22c), a slightly different grain distribution is obtained as compared with the case of solid movement but without grain tracking (Figure 22b).

Figure 23 shows the effect of grain movement on the local liquidus temperature. It is seen that for the two cases when the grain movement is not tracked, the variation of the local liquidus temperature is very close. The grain movement affects the local grain density (as shown in Figure 17), as well as the local temporal solid fraction and the Si concentration. Thus, the liquidus temperature is changed because of grain movement. Furthermore, the grain movement will make the solidification interval of each position different.

From the computed cooling curves, the local liquidus temperature, and fraction solid distribution, it is seen that the solid particle movement driven by natural convection and solidification contraction has significant influence on solidification characteristics and on the microstructure.

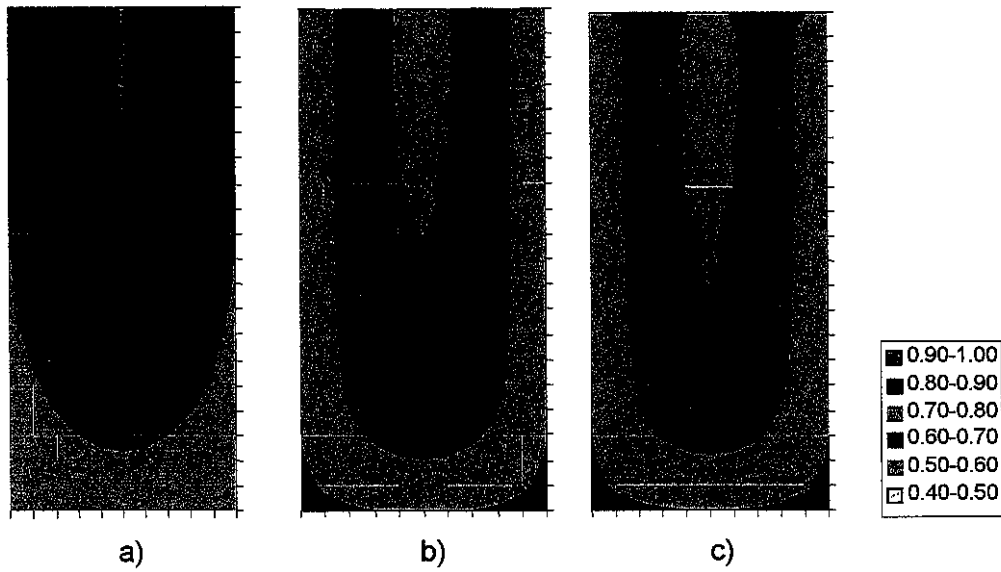


Figure 22 Final distribution of fraction of equiaxed dendrites in alloy A356 for different calculation conditions: a) no solid movement, liquid flow; b) solid and liquid flow, no grain tracking; c) solid and liquid flow, grain tracking

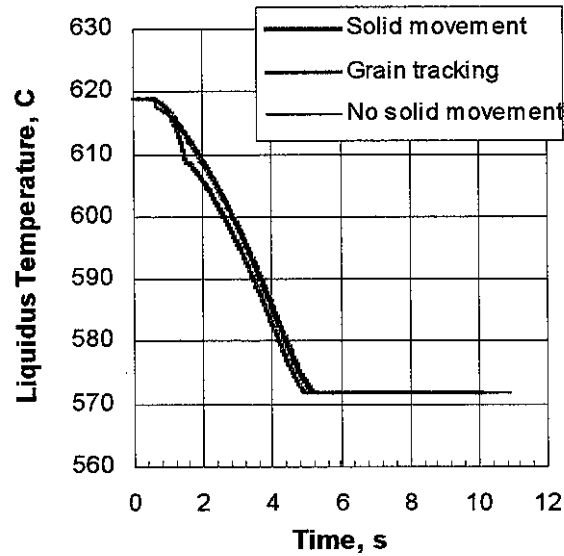
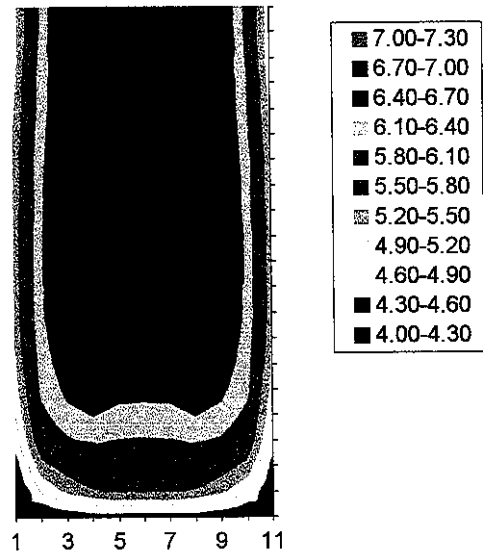


Figure 23 Temporal evolution of liquidus temperature at position B in Figure 12

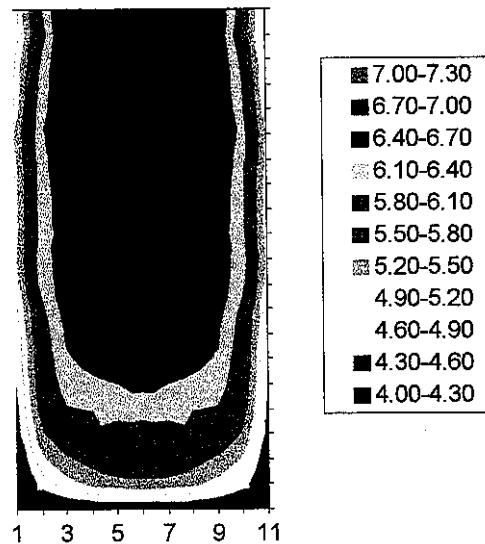
5.4 Comparisons

5.4.1 Nastac-Stefanescu model and Scheil model

The Nastac/Stefanescu (N-S) diffusion model and the Scheil model are used to calculate the solute distribution. The influences of natural convection, grain movement and solidification contraction on C_0 and f_s in both models are taken into consideration. The final average solute distributions for the D357 alloy are shown in Figure 24 for the N-S and Scheil model. It is obvious that both models predict similar concentration distribution except around the top of sample.



(a) N-S model



(b) Scheil model

Figure 24 Solute distribution for two diffusion models for D357 alloy

To show the capability of the program, the final solute composition along the centerline of the sample is plotted in Figure 25 for the N-S and Scheil models. A clear difference is seen at the top of the sample.

The evolution of liquid concentration along the centerline at different times is presented in Figure 26. It is seen that for any position within the casting the eutectic composition will be reached.

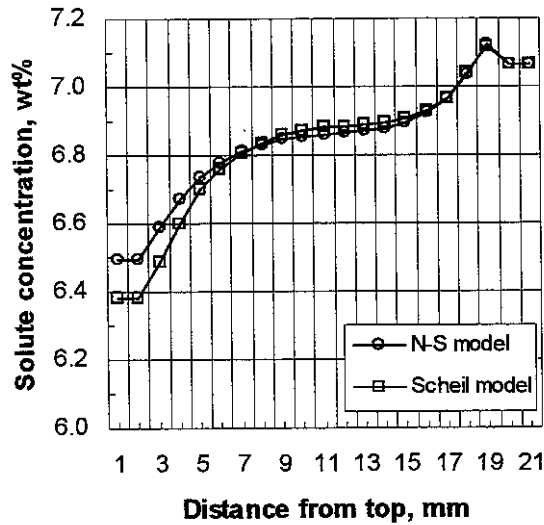


Figure 25 Final solute composition along the centerline of the sample

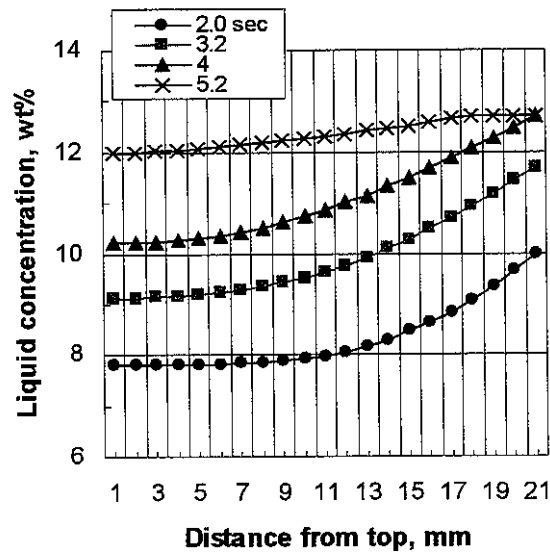


Figure 26 Liquid concentration along the centerline at different times

The relationship between the liquid concentration and the fraction solid at position A is shown in Figure 27. The data from this figure could be compared with the data from the phase diagram to illustrate the difference between equilibrium and non-equilibrium solidification.

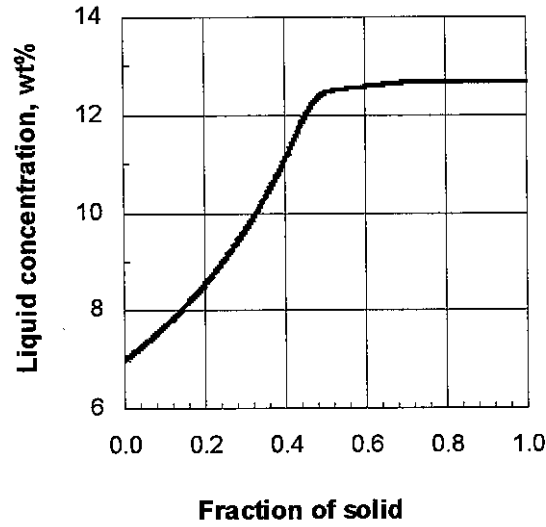


Figure 27 Relationship of liquid composition with solid of fraction at position B in Figure 12

5.4.2 Between A356 and D357

Although the two alloys are both Al-Si-Mg alloys, the difference in chemical composition is that the D357 alloy has a higher magnesium content, but does not contain Cu and Zn, which are present in A356 alloy. Moreover, the partition coefficient in the D357 alloy is a function of liquidus temperature, while it can be approximated to a constant in the A356 alloy, as shown in Figure 10.

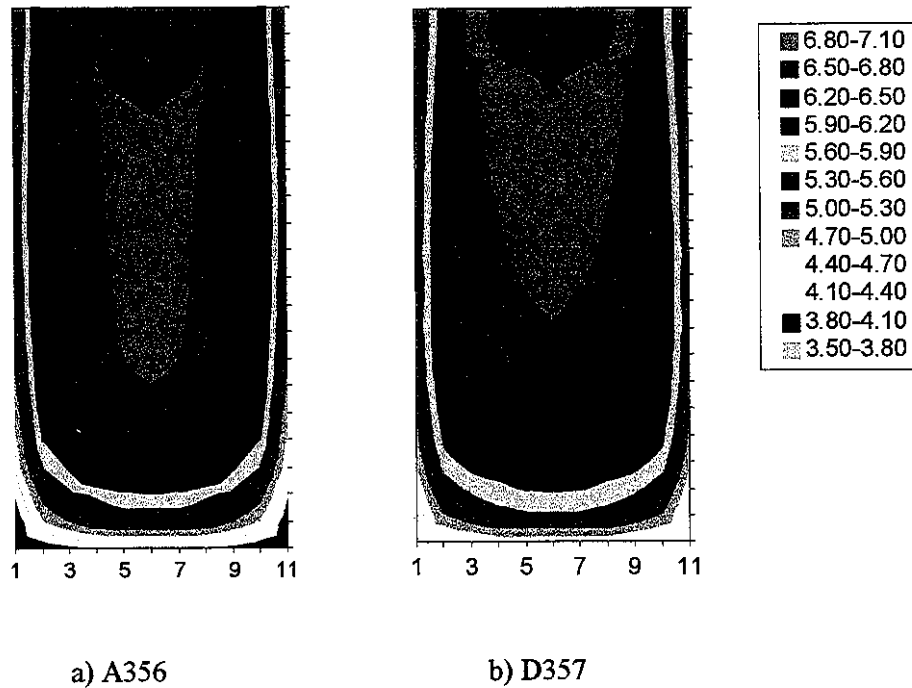


Figure 28 Final distribution of %Si in the computational domain

The cooling curves for both alloys are very similar, and the evolution of the solid fraction during solidification also compares well. However, the final Si distribution for these alloys is different, as illustrated in Figure 28. It can be seen that the location with highest Si content is not in the last region to solidify. This is because of convection and grain movement. The macro-segregation of Si is different mainly because of different partition coefficients. Thus, the micro-modeling of microstructure evolution is sensitive to the specifics of the alloys.

6. Possible model improvements

6.1 Consideration of the eutectic modification process

Based on the available experimental results for Al-Si alloys, the growth coefficient has been found to vary roughly between $10^{-6} \text{ m}\cdot\text{s}^{-1}\cdot\text{K}^{-2}$ for a slightly modified structure and $10^{-7} \text{ m}\cdot\text{s}^{-1}\cdot\text{K}^{-2}$ for a fully modified eutectic^{13,14,15}. These values were obtained through metallographic measurements and cooling curve analysis. In general, the growth coefficient decreases as the degree of modification increases and the degree of modification increases during eutectic solidification because the modifiers such as strontium and sodium gradually poison the silicon interface. To account for the progressive poisoning of the silicon interface during the eutectic solidification and the transition of the growth behavior from the lamellar to the fibrous, the following equation was introduced¹⁶:

$$\text{Eq. 39} \quad \mu = \mu_{rod} + (\mu_{lam} - \mu_{rod}) \exp\left(\frac{Vt^{1/2}}{D^{1/2}}\right)$$

where μ_{lam} is the initial growth coefficient (the order of magnitude of the lamellar eutectic is $10^{-5} \text{ m}\cdot\text{s}^{-1}\cdot\text{K}^{-2}$) and μ_{rod} the growth coefficient of the fibrous eutectic (the order of magnitude is 10^{-7}), t is the time when the eutectic solidification starts. The factor $V/D^{1/2}$ has been used to account for the opposite effects of interface velocity and diffusion in the liquid on the sodium or strontium segregation ahead of the liquid-solid interface. Although Eq. 39 is a first approximation, it reflects the micro-behavior to a certain extent.

The exact data in Eq. 39 will be measured in some future physical experiments. If we assume that $\mu_{lam}=1.0\cdot 10^{-5}$ and $\mu_{rod}=3.5\cdot 10^{-7}$ based on the existing experimental work¹⁶, then, the typical variation of the growth coefficient during the eutectic reaction is as shown in Figure 29.

A comparison of calculation using a constant and a variable growth coefficient is given in Figure 30. The cooling curves are calculated for position A within the test casting. The assumption of the pseudo-binary alloys was used. According to the existing experimental results¹⁷, if the Al-Si melt is fully modified, a larger undercooling is exhibited. No recalescence is observed. To our satisfaction, it is seen that the cooling curve shows no recalescence and the undercooling remains very large during the eutectic plateau when using a variable coefficient. Some recalescence occurs when a constant growth coefficient ($=3.5\cdot 10^{-7}$) is employed. Thus, the calculated cooling curve is sensitive to the growth coefficient.

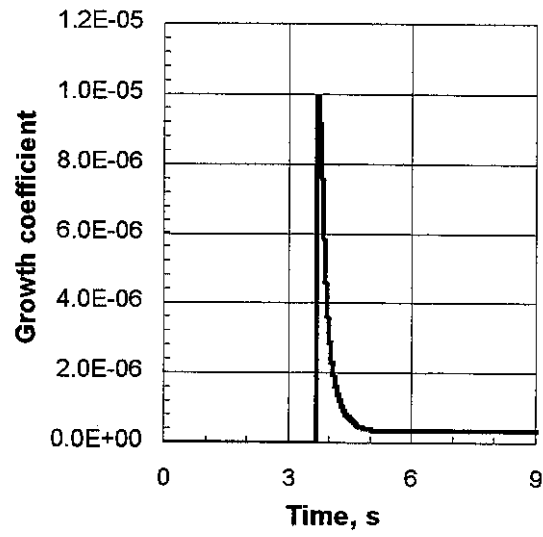


Figure 29 The variation of the growth coefficient during eutectic reaction

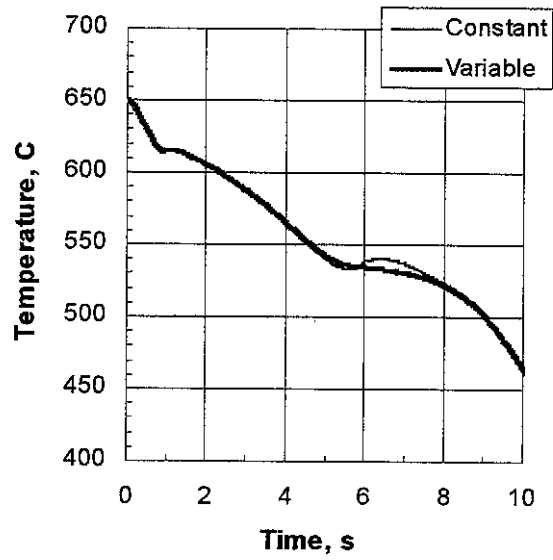
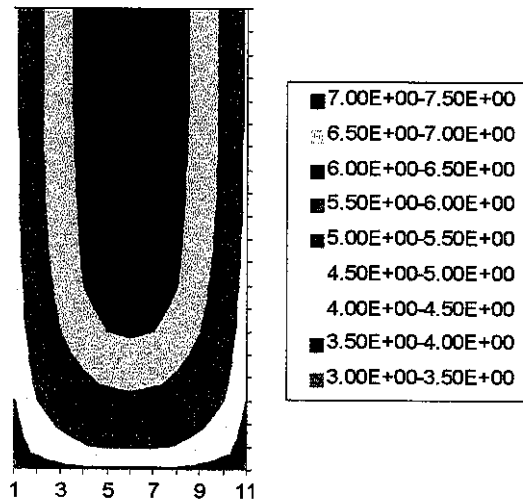
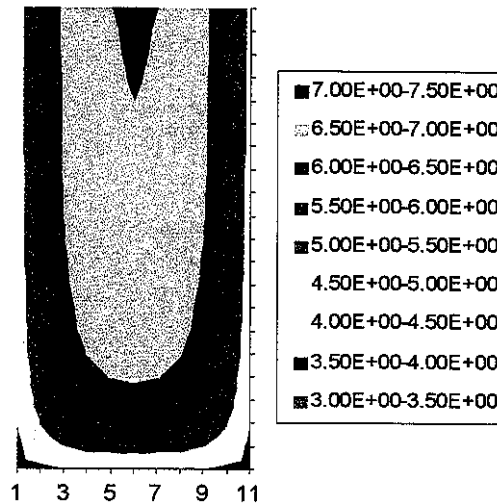


Figure 30 Cooling curves using a constant and variable growth coefficients for an A356 alloy



(a) with a constant coefficient



(b) with a variable coefficient

Figure 31 Final %Si distribution

Using the N-S model for the dendritic grain growth and setting C_0 to keep the initial value (7%Si), the computed result for the final average solute distributions are shown in Figure 31 for variable and constant growth coefficient. It is seen that segregation is positive. There is no negative segregation, but the area with high concentration is not same for the two cases. This further confirms that the growth coefficient has a significant influence on the final solute distribution.

6.2 Nucleation and growth of dendritic grains

The first nucleation of dendritic grains starts just when the temperature of the melt falls below the liquidus temperature. Before occurrence of recalescence (before point A in Figure 32a), the dendritic grains continue to generate and grow. When the cooling rate dT/dt becomes ≥ 0 , nucleation stops, and only the growth of dendrites occurs (from point A to Point B in Figure 32a). After the temperature decreases again below the last lowest temperature (point A), secondary nucleation starts. If we assume that the nucleation law has the same form for the first and second nucleation stages, the second nucleation stage would produce a much larger grain density than the first nucleation stage. According to our experimental observation this is not true.

As a first approximation, we assume the nucleation process of dendritic grains as follows:

- (1) dendritic grains begin to nucleate as soon as the temperature decreases below the initial liquidus temperature of the alloy and continues as long as the first condition, $dT/dt \geq 0$ is satisfied; this is point A on the cooling curve shown in Figure 32a;
- (2) when $dT/dt \geq 0$ there is no nucleation, but the existing dendritic grains continue growing;
- (3) secondary nucleation occurs when the temperature falls below the previous lowest temperature; this is from point B downward on the cooling curve shown in Figure 32a;
- (4) the nucleation process stops when dendrite coherency is reached; from this moment, the solidification process enters the second stage;
- (5) dendritic grains continue to grow until the end of solidification;

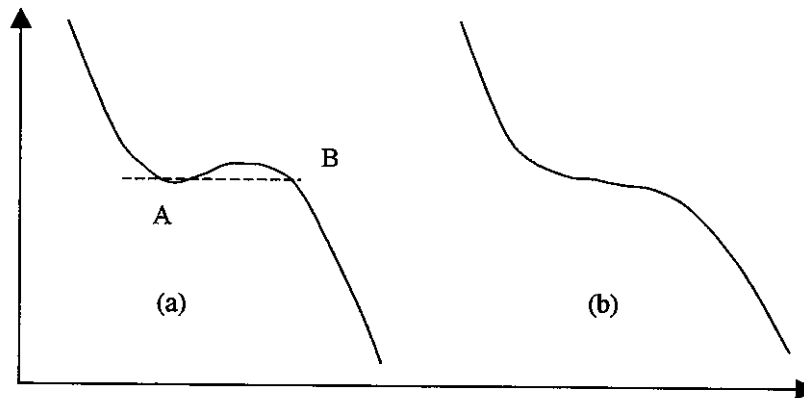


Figure 32 Illustration of nucleation of dendrites

- (6) if there is no recalescence on the cooling curve, as shown in Figure 32b, that is, dT/dt is always less than zero, nucleation until dendrite coherency is reached; the growth process of dendrites goes to the end of solidification.

6.3 Average grain size

In our proposed model, each volume element has a grain size distribution. To present the grain size distribution over the whole test sample it is necessary to use the average grain radius. It was derived that the average grain radius can be expressed as:

Eq. 40

$$\bar{r} = R_{\max} - \frac{\sqrt{3}}{3}(R_{\max} - R_{\min})$$

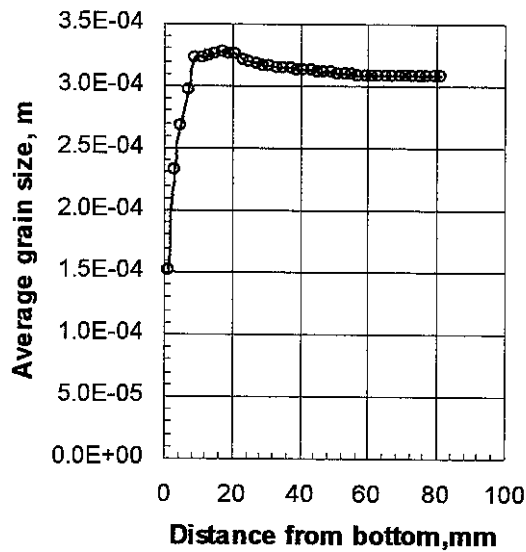


Figure 33 shows the final distribution of average grain radius along the central line of the test sample. Figure 34 demonstrates the final average grain radius distribution on the whole test sample. The position with small grain size has a relatively large volumetric grain density.

Figure 33 Distribution of average equiaxed dendritic grain radius along the central line of the test sample

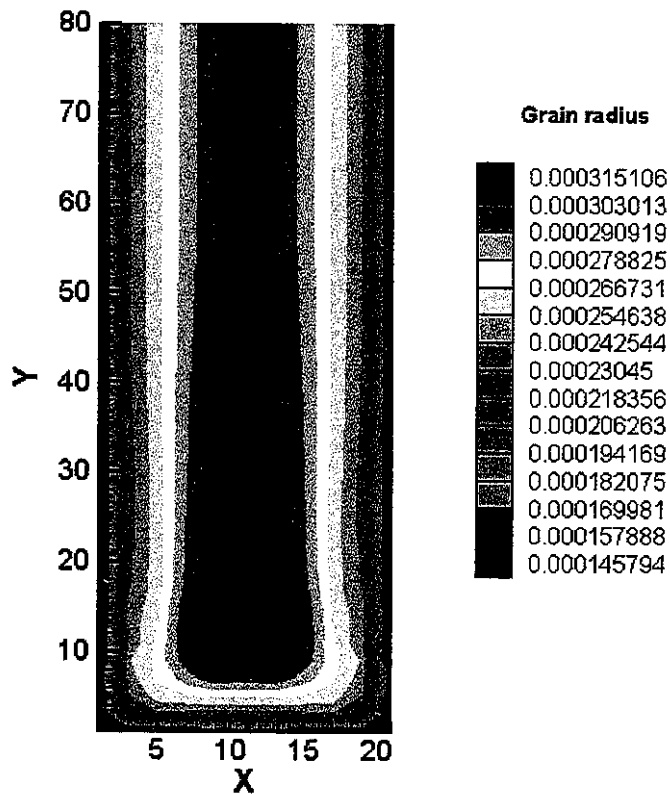


Figure 34 Distribution of dendritic grain size (size in m)

7. Experimental evaluation

7.1 The first test casting and instrumentation

The model developed so far is two-dimensional and is yet to be extended to deal with three-dimensional castings. The code for three-dimension will be developed in the next stage.

To determine the computational domain necessary in the central cross-section we designed an experimental test sample as shown in Figure 35. Three thermocouples were positioned on the central section of the sample. The positions for temperature measurements were 20mm, 30mm and 40mm from the bottom of sample, respectively. The thermocouples were placed on a symmetric plane within the sample in the y-direction. Thus, the net heat flux in the y-direction from this plane was zero. Nevertheless, the boundary conditions of the casting in the z-direction are different. The position in the z-direction where the temperature gradient can be approximated to be zero, must be experimentally determined. The test casting beyond this zero gradient can be ignored for computational purposes. The plane that separates the zero gradient zone from the rest of the test casting can be considered as an insulated surface in the numerical calculation.

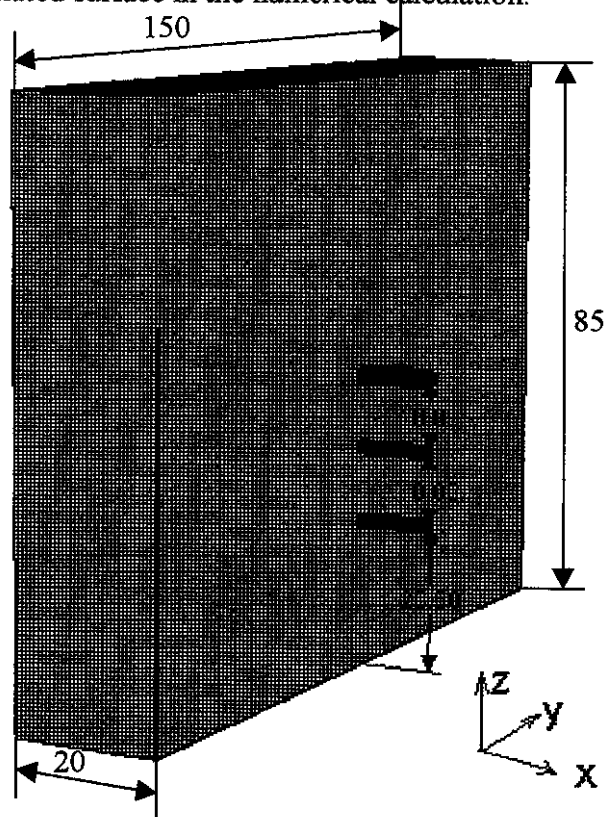


Figure 35 The first pepset molded test sample and thermocouple positions

7.1.1 Cooling curves and discussion

The test sample of A356 alloy was poured in a Pep-set™ mold. The measured cooling curves at the positions shown in Figure 35 are plotted in Figure 36. It is seen that the cooling curves still show no visible recalescence during the eutectic transformation since

the melt was fully modified (0.015%Sr). The behavior of cooling curves at all three positions is very similar, and their values are also very close. The maximum difference between them is less than 3°C during the entire solidification. The temperature distribution indicates that the temperature gradient from 20 mm to 40mm in the z-direction is near zero. The computational domain finally selected is 20mm wide and 30mm high.

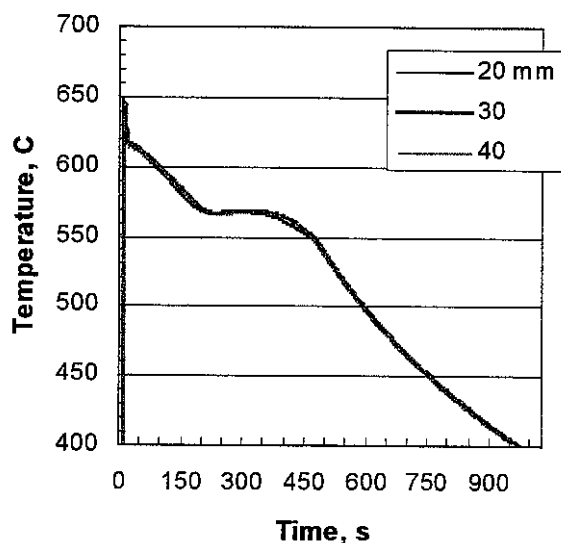


Figure 36 Cooling curves at different positions

From the measured cooling curves, the total solidification time is around 500 seconds. If we take this case to be a physical model to simulate the solidification process, the calculation will need a long time, and it could make the mold interrogation work slowly. To overcome the problem, a thinner casting sample was poured in the Pep-set mold for cooling curve measurements, and a metal mold, required for further experiments was designed.

7.2 The second test casting in the sand mold

7.2.1 Casting sample and thermocouple positions

The dimensions of the test sample were as follows: 150mm long, 85 mm high and 15mm thick. The position of the five thermocouples is illustrated in Figure 37. Four thermocouples (1 –4) were positioned on the central axis of the sample at different distances from the bottom (13mm, 18mm and 28mm). To confirm that there is no temperature gradient in the length direction, two thermocouples (2 and 4) were positioned 18 mm from the bottom but 10 mm apart in the length direction. Another thermocouple (5) was placed at the surface of the sample and at 18 mm from the bottom.

Nevertheless, the boundary conditions of the sample in the height direction were different. The position along the height direction, in which the temperature gradient can be approximated to be zero, must be experimentally estimated. For this sample, it is still necessary to determine the height of the computational domain.

7.2.2 Cooling curves and discussion

An A356 alloy melt was melted in a resistance furnace, and held at a temperature of 760 °C for degassing and modification. Argon gas was used to degas the melt. Grain refinement was induced through the addition of 0.1% Ti in the form of a 5/1-type master alloy (5Ti:1B). Eutectic modification was done by adding 0.02% strontium.

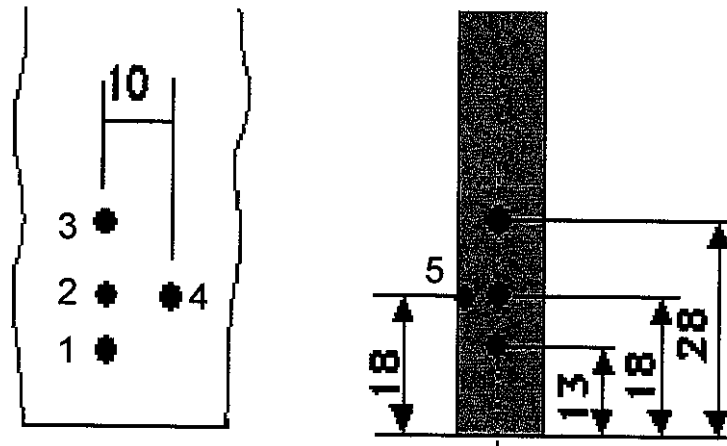


Figure 37 The second pepset molded test sample and thermocouple positions (units mm)

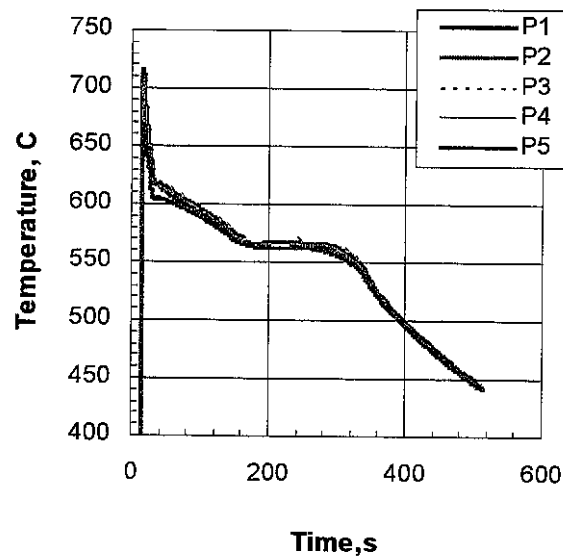


Figure 38 Cooling curves at five different positions

The melt was poured in a Pep-set mold at a pouring temperature of 740 °C. The measured cooling curves at different positions are shown in Figure 38. It is seen that no visible recalescence occurs during either primary or eutectic solidification. This demonstrates that grain refinement and modification were correctly conducted. The cooling curves for thermocouples 1-4 are very similar. Higher undercooling is recorded for thermocouple 5 positioned at the wall. The maximum temperature difference between thermocouples 1-4 is less than 3 °C. This indicates that the temperature gradients in the length and height

directions are nearly zero. Thus, a domain having a height of 20 mm was used for computation. For this domain an insulated surface boundary condition can be assumed for the top surface (since there is no temperature difference between thermocouples 1, 2, and 3). The cooling rate above the liquidus temperature, measured at 617 °C was about 4-5 °C/s. The temperature of eutectic arrest was 563-567 °C for the four positions at the central plane (1-4), and 560 °C for the surface thermocouple (5).

7.2.3 Macrostructure and Microstructure

The macrostructure of the A356 samples is shown in Figure 39 and Figure 40. In both cases the structure is equiaxed with no columnar grains. A higher magnification picture for the second sample is shown in Figure 41. The maximum radius of primary dendrites is about 0.5 mm.

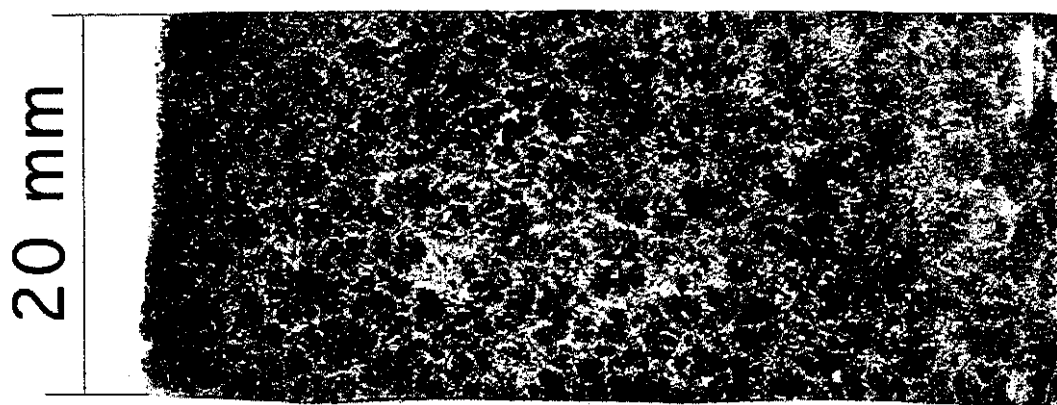


Figure 39 Macrostructure of the first A356 sample without grain refiner

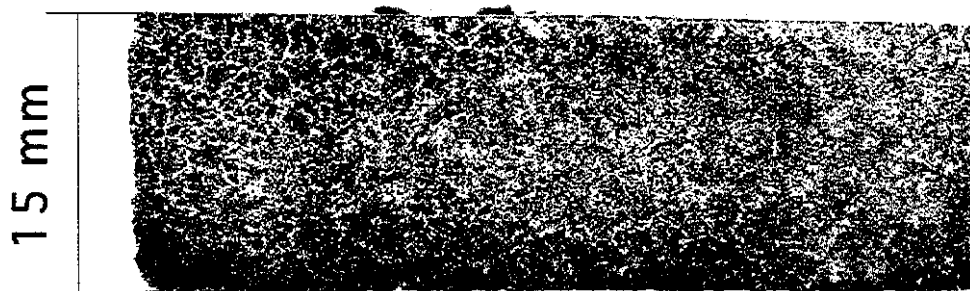


Figure 40 Macrostructure of the second A356 sample

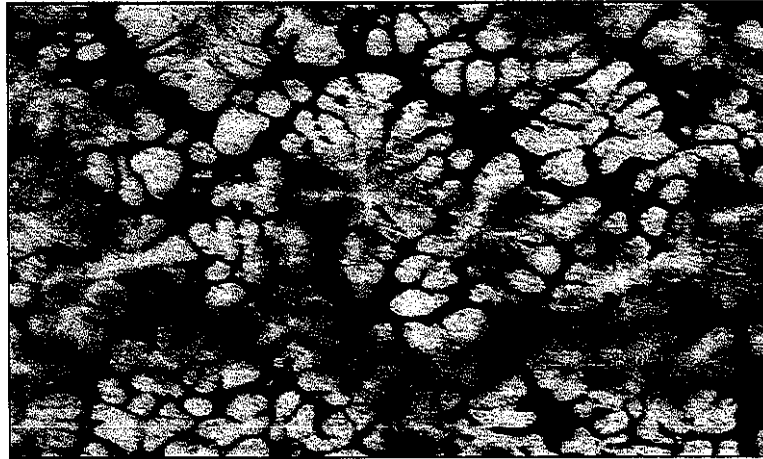


Figure 41 Microstructure of A356 sample

When comparing the grain size of this sample in Figure 40 with that of the sample poured in the first sand mold (Figure 39), it is seen that a finer grain size was obtained through the use of the grain refiner.

7.3 Samples poured in a metal mold

The cooling rate of the casting in the Pep-set mold is relatively low. Thus, the solidification times of the test samples were 500 seconds for a 20 mm thick casting, and about 320 seconds for a 15 mm thick casting. If only this resin-bonded sand mold would be used, in the present stage of model development two negative consequences will result. Firstly, a long calculation time is required. Secondly, the experimental results at relatively high cooling rate are not available. Consequently, a new cast iron mold was designed and made.

7.3.1 The first metal mold and its instrumentation

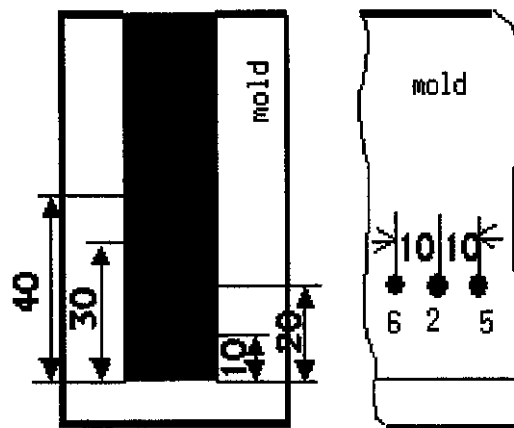


Figure 42 Mold instrumentation (Units: mm)

The dimensions of the sample casting are 110 mm long, 90 mm high and 20 mm thick. As a first approximation, the six thermocouples were placed in the mold as shown in Figure 42. Four thermocouples (1-4) were positioned on the central axis of the sample at

different distances from the bottom (10, 20, 30, 40 mm). Thermocouple 5 was placed at the surface of the sample and 6 was at 5 mm depth from the surface of the sample. Both no. 5 and 6 thermocouples were positioned 20 mm from the bottom. They were set 10 mm apart in order to avoid interference.

7.3.2 Typical Cooling curves in the metal mold

An A356 alloy was melted in a resistance furnace, and held at a temperature of 760 °C for degassing and modification. Argon gas was used to degas the melt. 0.1%Ti in the form of 5/1-type master alloy (5Ti:1B) was introduced in the melt as grain refiner, and 0.02% Sr in the form of 10%Sr master alloy was added into the melt as modifier.

In the first test, the metal mold was not preheated. The melt was quickly poured in the metal mold at 730 °C. The measured cooling curves at different positions are shown in Figure 43. It is seen that the total solidification time was only 35 seconds and no visible recalescence appears during either the primary dendritic or the eutectic solidification. This behavior of cooling curves demonstrates that grain refinement and modification were correctly conducted.

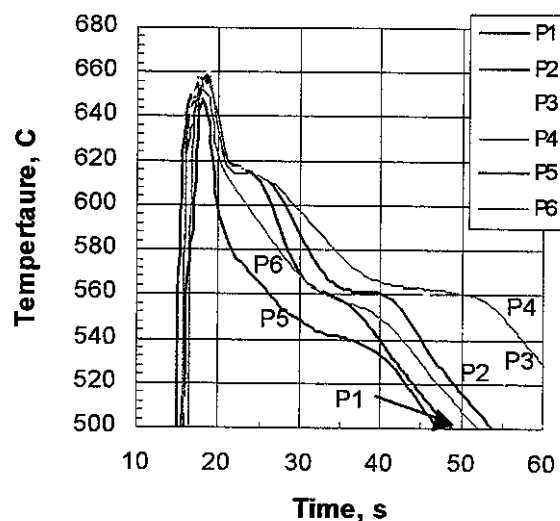


Figure 43 Cooling curves at different position of the sample

From the measured cooling curves, different starting temperatures of solidification were found at the different positions from the bottom of sample (1-4); also, different eutectic temperatures were recorded. These phenomena have not been clearly observed in the samples poured in the Pep-set mold before. The cooling rates measured immediately above the start of solidification were 17-20 °C/s for thermocouples 1 to 4. Comparing data from thermocouple 1 (bottom) and 4 (top), the difference in the starting temperatures of solidification is about 5 °C. Furthermore, the eutectic arrests for all six thermocouples were not the same.

According to the current experimental data, the cooling rate at the surface of the sample is around 24 °C/s. To obtain reliable data, the same measurement should be repeated at a high frequency of data acquisition, and with more thermocouples.

7.3.3 Microstructural observation

The sample poured in the metal mold was polished, and etched with Keller's reagent, and then observed under an optical microscope equipped with an image analyzer.

The microstructure images at positions corresponding to the thermocouples 1 to 4 are presented in Figure 44. An equiaxed structure with no columnar grains is seen. It was also found that the number of equiaxed dendrites per unit area or grain density along the central line of sample is different although the cooling rates at positions from 20 to 40 mm from the bottom of the sample are close. They correspond to the thermocouples 2 to 4. However, the number of dendrites at the position 10mm from the bottom, which corresponds to the thermocouple 1, is higher than that at other locations (2 to 4) along the central line of sample.

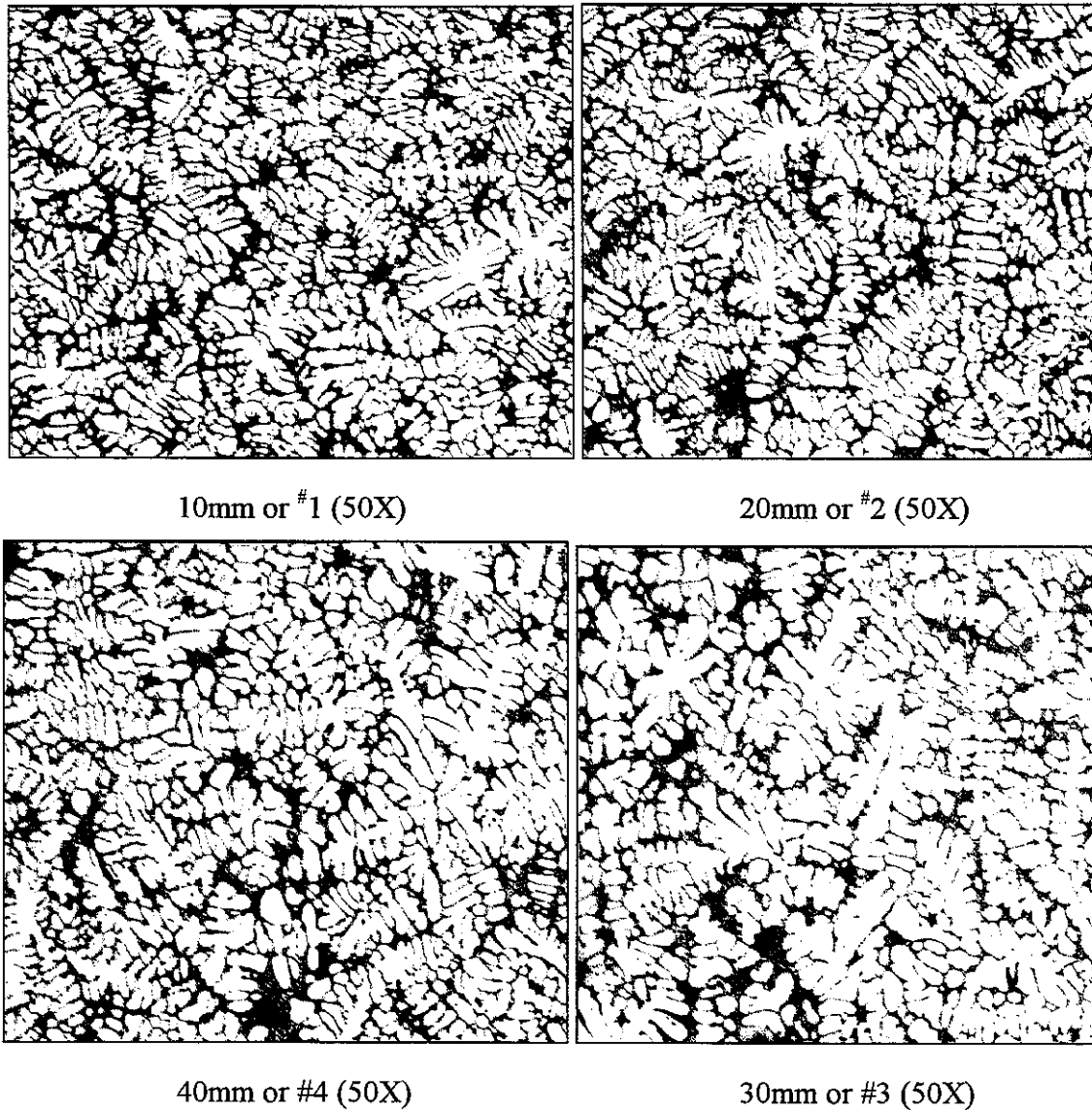
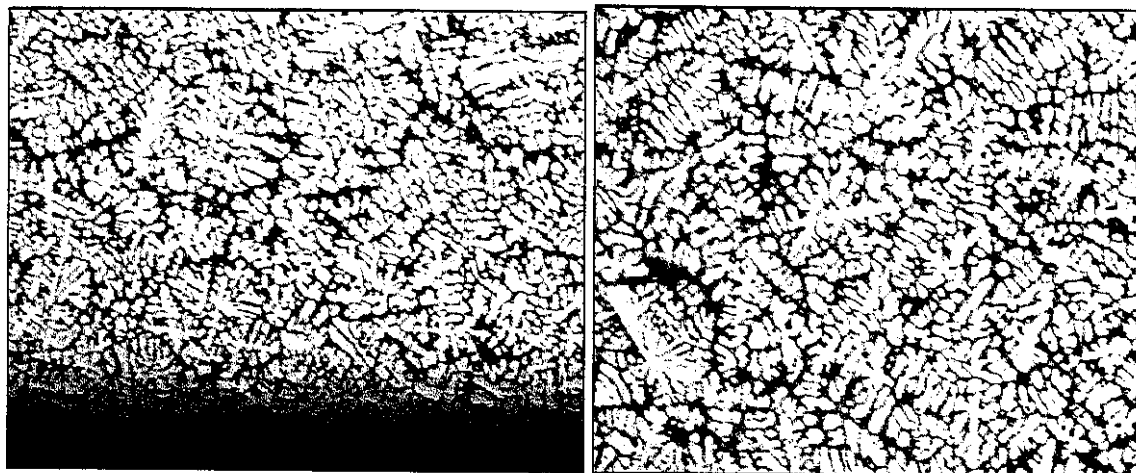


Figure 44 Dendritic grains along the centerline of sample and at different positions from the bottom

The microstructure images at the surface and the 5 mm depth from the surface of the sample can be seen in Figure 45. The number of the primary equiaxed dendrites is very high and the grain size becomes smaller at the surface. The grain density is relatively lower than that near the surface of the sample. As expected, the higher cooling rates produce high grain density and smaller grains.



Surface or 5 (50X)

5mm from surface or 6 (50X)

Figure 45 Dendritic grains at the positions of the surface and sub-surface of sample

We observed that the number of equiaxed dendritic grains per unit area not only depends on the local cooling rate, but also that the grain movement could significantly influence distribution of grain density.

7.3.4 Thermal analysis

Another A356 alloy was melted in a resistance furnace, and held at a temperature of 760 °C for degassing and modification. Argon gas was used to degas the melt. 0.1%Ti in the form of 5/1-type master alloy (5Ti, 1B) was introduced in the melt as grain refiner, and 0.02% Sr in the form of 10%Sr master alloy was added into the melt as modifier. The metal mold was held at room temperature before pouring.

The casting sample had the same dimensions as in the last report (110 mm long, 90 mm high and 20 mm thick). In this measurement, the eight thermocouples were instrumented in the mold as shown in Figure 46. All thermocouples were set 10 mm apart in order to avoid interference. Six thermocouples (1-6) were placed on the central axis of the sample at different distances from the bottom (10, 20, 30, 40, 50, 60 mm). Thermocouple 7 was positioned at the surface of the sample and no. 8 was at 5 mm depth from the surface of the sample. Both 7 and 8 thermocouples were positioned 20 mm from the bottom.

The measured cooling curves at different positions are shown in Figure 47. It is seen that the general trend of the cooling curves is the same as in the previous measurement. This demonstrates that the melting and treatment of the melt were correctly conducted.

According to the first derivative of the cooling curves, different nucleation temperatures were found at different positions from the bottom of sample (1-6). Comparing data from thermocouple 1 (bottom) and 6 (top), the maximum difference of the nucleation

temperature is about 3 C for primary dendrites. The cooling rates measured from Figure 48 immediately before the nucleation temperature were 9.1-11.2 C/s for thermocouples 1 to 6. Different start temperatures were found for the eutectic transformation at different locations. A typical cooling curve and the first derivative curve at Point 2 is shown in Figure 49. Based on the analysis of the first derivative curves and corresponding cooling curves, the significant temperatures were summarized in Table 8.

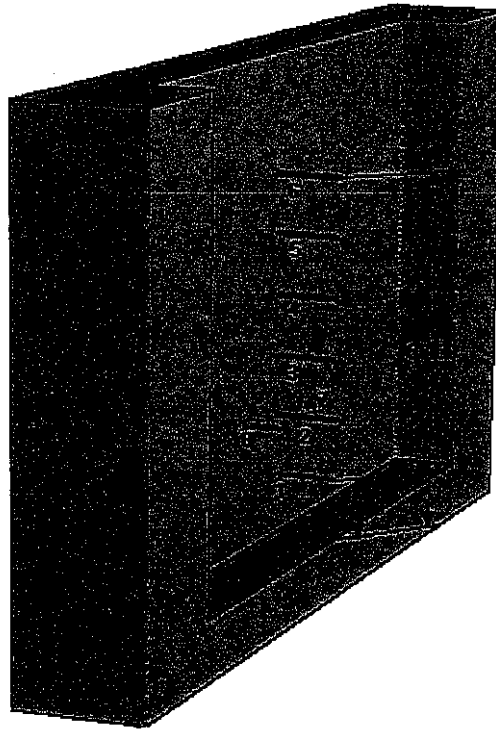


Figure 46 Mold instrumentation (Units: mm)

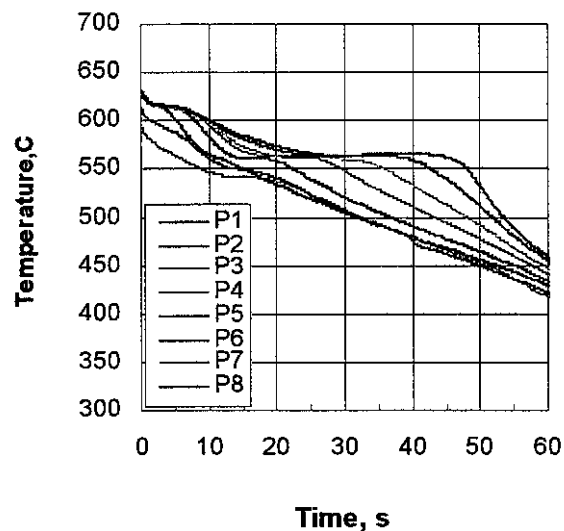


Figure 47 Cooling curves at different position of the sample

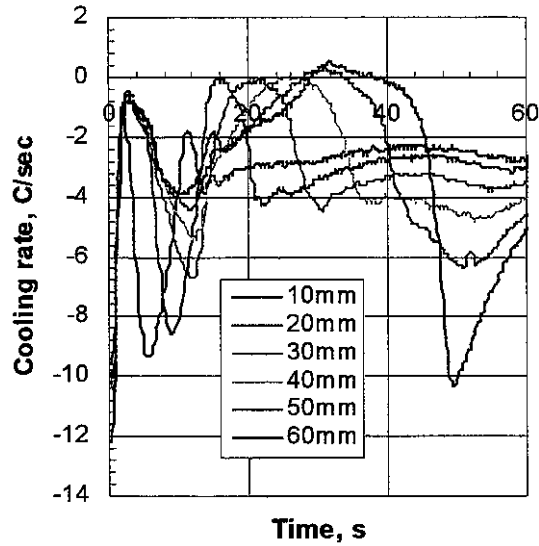


Figure 48 The first derivative curves of the thermocouples 1-6 (10mm-60mm)

Table 8 Results of thermal analysis

Position (mm)	10	20	30	40	50	60
T_g (dendrites)	615.5	614.3	616.7	613.7	616.4	616.5
dT/dt	10.5	11.2	9.9	10.2	10	9.1
T_G (eutectic)	560.6	561.4	562.7	560.7	562.8	563.1

* T_g is steady state growth temperature of the melt during primary dendrites

* T_G is steady state growth temperature of the melt during eutectic (see Figure 49)

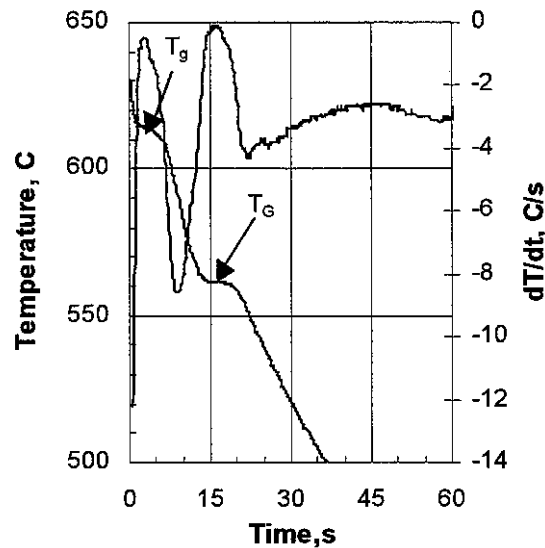


Figure 49 The first derivative and its cooling curve at Point 2 (20mm)

It should be mentioned that the cooling rates shown in this experiment are different from that obtained in the last experiment because of mold coating thickness and pouring temperature. Unfortunately, the cooling rate at the surface of the sample was not recorded due to relatively low pouring temperature.

7.4 Measurement of grain density

The grain density was measured on the samples poured in the sand mold and metal mold. The grain density measured directly on the screen of image analyzer is defined as the number of dendrites per unit area. The volumetric grain density can be obtained from the following formula¹⁸:

$$\text{Eq. 41} \quad N_v = 0.87 \cdot N_s^{1.5}$$

where N_s is grain density per unit area, and N_v is grain density per unit volume.

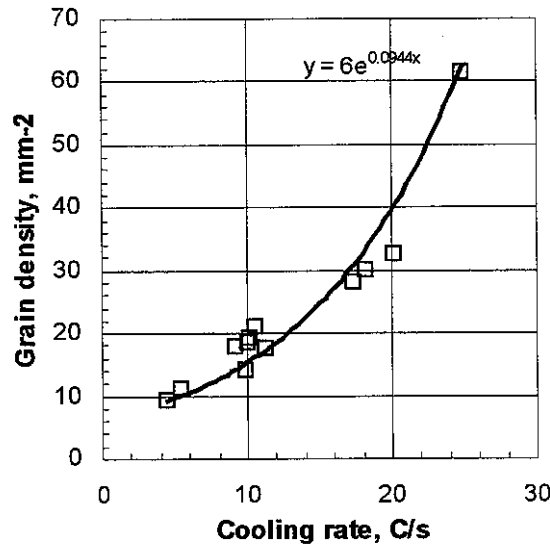


Figure 50. Variation of grain density with cooling rate

In the present experimental measurements, an equiaxed structure with no columnar grains was obtained. The samples poured in the sand mold and the metal mold were polished, and etched with Keller's reagent. Three images were observed under an optical microscope equipped with an image analyzer, and selected around each position that corresponds to the specific thermocouple or cooling rate. The average of three measurements on the same position was used. The summary of experimental results of measurements on the grain density is shown in Figure 50, and the corresponding volumetric grain density profile is plotted in the same figure. It is seen that, as expected, the grain density increases with increasing cooling rate. However, the grain density is more sensitive to cooling rate when the cooling rate is higher than 20 C/s.

Based on the collected data from several experiments, the correlation between the grain density (2D), N_s , and cooling rate, \dot{T} , can be expressed as:

$$\text{Eq. 42} \quad N_s = 6 \cdot \exp(0.0944 \dot{T})$$

7.5 Quenching experiment and microstructure observation

Another A356 alloy was melted in a resistance furnace, and held at a temperature of 760 C for degassing and modification. Argon gas was used to degas the melt. 0.1%Ti in the form of 5/1-type master alloy (5Ti:1B) was introduced in the melt as grain refiner, and 0.02% Sr in the form of 10%Sr master alloy was added into the melt as modifier. Cylindrical bars were poured into the graphite mold. The bars were machined to the desired size. The solidified bars were remelted in a ceramic crucible using a high frequency induction furnace. The temperature was recorded with a data acquisition system. The bar was heated to about 650 C in the ceramic crucible. After soaking for 10 minutes, the furnace was turned off or kept at a reduced power level and the melt was cooled inside the furnace. At a desired undercooling, the crucible was quenched in cold water. The cooling rate of solidification can be controlled by changing the material of the crucible holder, as well as the power level of the furnace.

A testing sample was quenched at 615 C. The microstructure of the quenched sample is shown in Figure 5. The water-quenched sample was polished, etched with Keller's reagent, and then the microstructure images were observed under an optical microscope equipped with an image analyzer. An equiaxed structure with no columnar grains was obtained. In the present experiment, no micro-porosity or pores were found in the etched sample though we did not degas again the melt in the crucible before quenching.

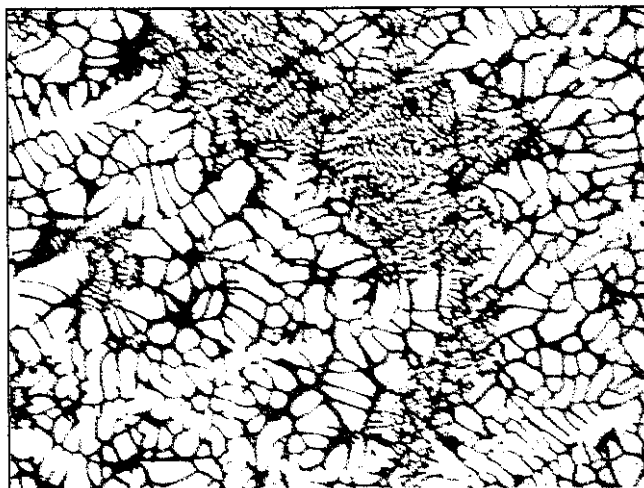


Figure 51 Microstructure of quenched sample, 50X

From Figure 51 we can see the two types of dendrites. The large ones formed before quenching. The small ones occurred during quenching. The length scale of the dendrites formed before quenching are associated with a specific undercooling.

The equipment must be modified for better control of the cooling. This is yet to be completed.

7.6 Visualization of eutectic grains

The eutectic grain density measurement is critical to obtain the nucleation law for eutectic grains during the eutectic transformation. An Al-12.7Si binary alloy was poured in the same metal mold used for producing A356 samples. The cooling curves for the Al-Si

binary alloy with 12.7 Si wt% are shown in Figure 52 (see Figure 46 for position of thermocouples). Although the exact eutectic composition was chosen to develop the etching method for the visualization of the eutectic grains, primary dendrites occurred because the test sample was poured in a metal mold. This is confirmed by the existence of primary arrest on Figure 52. The fact demonstrates that the eutectic composition does not keep its value on the equilibrium phase diagram under real casting conditions, but shifts to a higher Si content.

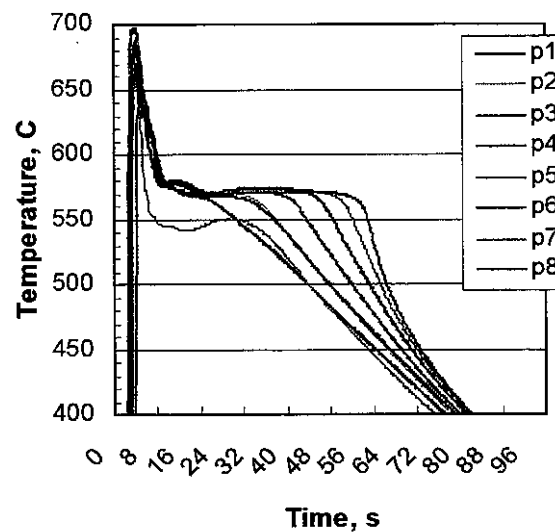


Figure 52 Measured cooling curves for Al-Si binary alloy with 12.7%Si

A metallographic investigation was carried out in order to outline the eutectic grain in Al-Si alloy. The samples were analyzed by chemical and thermal etching methods.

After grinding, the samples were roughly polished with diamond suspension, oil-based 1 micron, followed by final polishing with alumina suspension, water-based, 0.05 microns. The visualization of eutectic grains was based on the existing work in Ref.16.

7.6.1 Chemical etching

The reagent used is based on Poulton's etchant (60%HCl, 30%HNO₃, 5%HF, 5%H₂O). Special care has to be taken while preparing this etchant, because of its very high reactivity.

The sample is swabbed with cotton for several seconds, then rinsed in water. A slightly subsequent polishing has to be done with alumina suspension, until the grain boundary becomes shiny. The eutectic grains as well the primary dendrites are clearly shown in Figure 53(a), (b) and (c). It is seen that each eutectic grain contains several dendrites.

7.6.2 Thermal etching

The samples were held for 1 hour at 590 C, then immediately immersed in cold water and dried. Figure 54 clearly shows the eutectic grains through color tinting of the sample's surface.

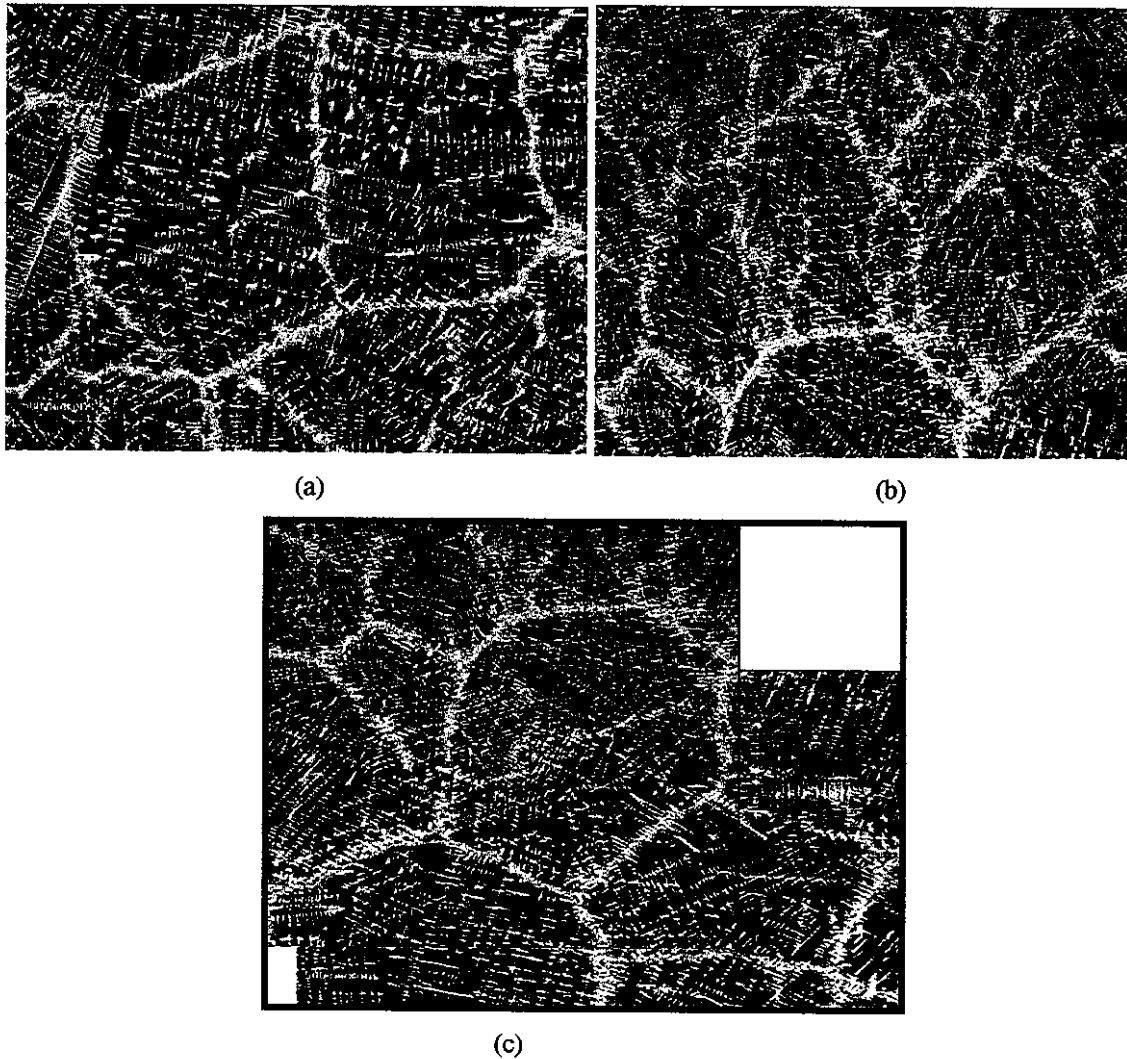


Figure 53 Outlining of eutectic grains using chemical etching (composition picture)

It was demonstrated that by using chemical and thermal etching methods, the eutectic grain density, size and other parameters can be measured to validate our proposed model. Note that the experimental variables for Al-Si alloy with 12.7% Si are not completely suitable for the multi-component alloy A356. We are still developing the method to show the eutectic grains for A356 alloy.

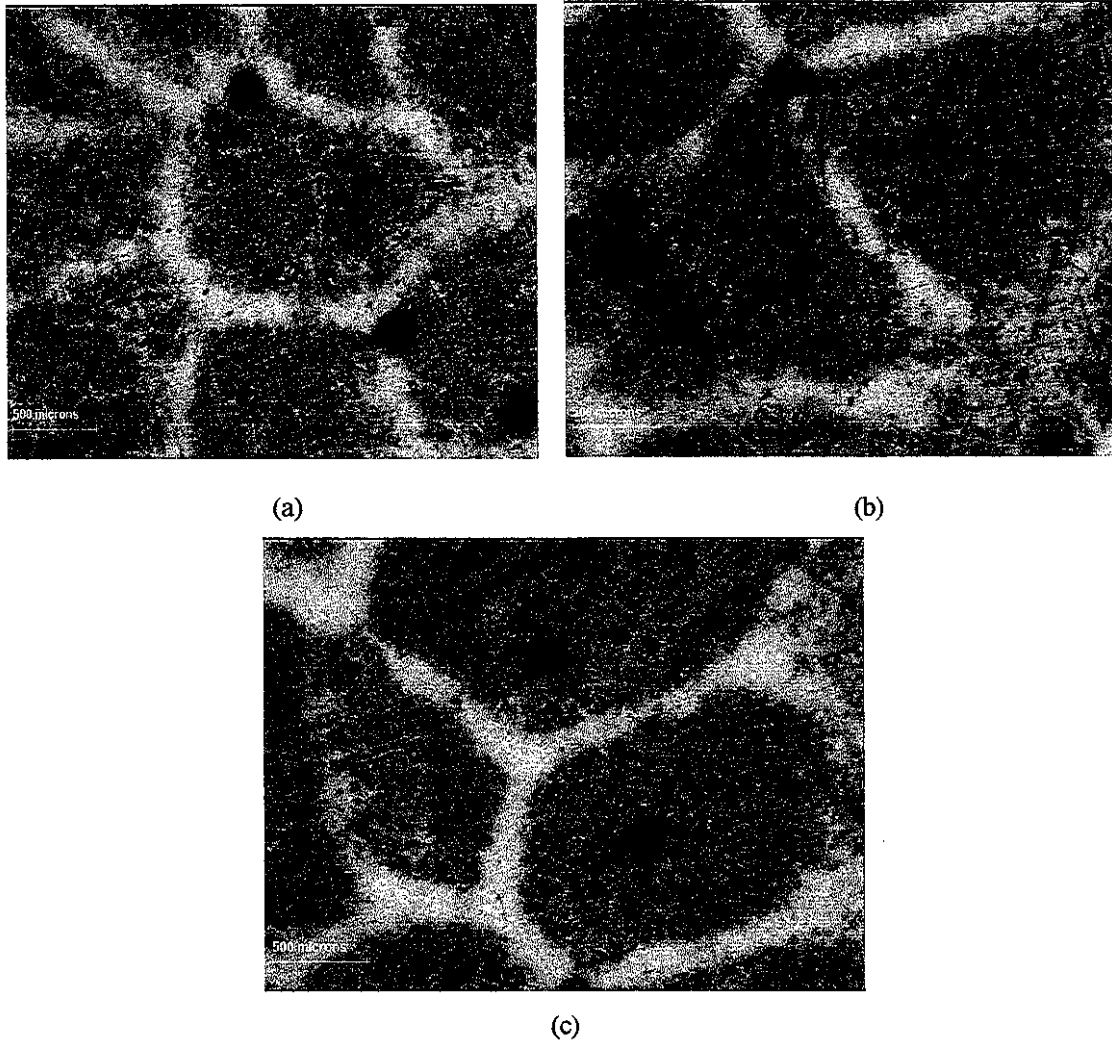


Figure 54 Outlining of eutectic grains using thermal etching

8. Conclusions

The work performed in the first year was focused on the development of a comprehensive model that could predict the microstructural evolution of A356 and D357 alloys. The proposed model has two basic components, macro-modeling and micro-modeling. Many phenomena that strongly affect the solidification behaviors of casting are considered, such as thermosolutal buoyancy, solidification shrinkage, nucleation and growth of grains, and grain movement.

The proposed model can account for the influences of natural convection, solidification shrinkage, continuous nucleation and growth, and grain movement on the microstructural evolution during solidification of multi-component alloys. It describes non-equilibrium solidification and the competitive growth. We have demonstrated that the model is capable of tracking grain movement during solidification. The model is suitable for the A356 and D357 alloys with equiaxed dendritic and eutectic morphology.

One of the most important contributions is that the model includes tracking of dendritic and eutectic grains during solidification, and that it eliminates the assumption of uniform grain size in a given volume element, which is standard in current solidification models.

Rules of grain movement were developed to track grain movement. The method allows tracking grain growth of continuously nucleated grains and their movement without using large amounts of computer memory. It is a practical approach that can be used for large castings where the number of control volumes is high.

The computed results demonstrate that the equiaxed grains can move freely with the melt and play an important role in the early solidification stage of casting. The tracking of grain movement is important to the accurate prediction of microstructural evolution and room temperature microstructure.

Significant amount of experimental work has been performed with the purpose of establishing correct nucleation and growth laws for dendritic and eutectic solidification in the multi-component alloys of interest (A356 and D357). However, more experiments are needed to complete this task.

9. Future work

Future work should address both modeling and experiment. For the modeling part, we would suggest the following main tasks:

- a) Modify the growth law for the eutectic grains.
- b) Modify the nucleation law to properly consider the contribution of the secondary nucleation to the solid fraction.
- c) Develop a program to solve liquid concentration in the mushy zone.
- d) Improve the calculation of segregation.
- e) Include modeling of shrinkage and void formation.
- f) Implement the proposed model and validate the computed results.
- g) Develop three-dimensional version to correctly describe solidification of commercial casting.

For the experimental part, we propose the following major tasks:

- a) Initiate quenching experiments for A356 and D357 alloys and measure the undercooling for each of samples.
- b) Develop a method to count the number of equiaxed dendritic grains.
- c) Establish a relationship between grain density and undercooling.
- d) Develop an approach to visualize the eutectic grains of A356 and D357 alloys, and count the number of the eutectic grains.
- e) Determine the coefficients of nucleation and growth law from the experimental results.
- f) Improve the experimental apparatus to achieve better control of cooling.

References

- ¹ W.D.Bennon and F.P.Incropera: Int. J. Heat Mass Transfer, 1987, Vol.30(10), pp2161-70 and 2171-87
- ² S.Chang and D.M.Stefanescu: Metallurgical and Materials Trans. A, 1996, Vol.27A, 2707-21
- ³ P.C.Carman: Trans. Inst. Chem. Eng., 1937, Vol.5, 150-66
- ⁴ S.V.Patankar and D.B.Spalding: Int.J. Heat mass Transfer. 1972, Vol.15, 1787-806
- ⁵ W.Oldfield: ASM Trans., 1966, Vol.59, 945-60
- ⁶ L.Nastac and D.M.Stefanescu: Metall. Materials Trans.A, 1996, Vol.27A, 4061-74
- ⁷ D.D.Goettsch and J.A.Dantzig: Metall. and Material Trans.A, 1994, Vol.25A, 1063-79
- ⁸ B.J. Yang, J. Leon-Torres, and D.M. Stefanescu, Int. J. Cast Metals Res., 1999, Vol.11, 527-32
- ⁹ D.M.Stefanescu: ISIJ International, 1996, Vol.35(6), 637-50
- ¹⁰ L.Nastac and D.M.Stefanescu: Micro/Macro Scale Phenomena in Solidification, ASME, 1992, Ed. C.Beckermann *et al*, 27-34
- ¹¹ D.B. Spalding, in Recent Advances in Numerical Methods in Fluids, ed. C. Taylor and K. Morgan, (Pineridge Press, Swansea, 1981), 1, 139-167
- ¹² W. J. Boettinger et al., in Modeling and Casting, Welding and Advanced Solidification Processes VIII, B.G. Thomas and C. Beckermann eds, TMS (1998) 159
- ¹³ J.A.E. Bell, W.C. Winegard, J. Inst. Metals, 1966, Vol.94., 222-27
- ¹⁴ M.G. Day, J. Ins. of Metals, 98(1970), 57-59
- ¹⁵ J.O. Barlow, D.M. Stefanescu, AFS Trans., 105(1997), 349-354
- ¹⁶ C.Degand, D.M.Stefanescu, G.Laslaz: Solidification Science and Processing. Ed. I.Ohnaka and D.M.Stefanescu, 1996, 55-63
- ¹⁷ Lennart backerud, Guocai Chai and Jarmo Tamminen: Solidification Characteristics of Aluminum alloys, Volume 2 Foundry Alloys, AFS, 1990
- ¹⁸ J.V.Dawson and W.Oldfield: BCIBA J., 1960, Vol.8, 221-31